Quark masses and low-energy constants in the continuum from the tadpole-improved clover ensembles

Zhi-Cheng Hu,[1,2] Bo-Lun Hu,[3] Ji-Hao Wang,[3,2] Ming Gong,[4] Guoming Liu,[5,6] Liuming Liu,[1,7,*] Peng Sun,[1,†] Wei Sun,[4] Wei Wang,[8,9] Yi-Bo Yang,[2,3,10,11,‡] and Dian-Jun Zhao[2,3]

(CLQCD Collaboration)

[1]*Institute of Modern Physics, Chinese Academy of Sciences, Lanzhou 730000, China*
[2]*University of Chinese Academy of Sciences, School of Physical Sciences, Beijing 100049, China*
[3]*CAS Key Laboratory of Theoretical Physics, Institute of Theoretical Physics, Chinese Academy of Sciences, Beijing 100190, China*
[4]*Institute of High Energy Physics, Chinese Academy of Sciences, Beijing 100049, China*
[5]*Key Laboratory of Atomic and Subatomic Structure and Quantum Control (MOE), Guangdong Basic Research Center of Excellence for Structure and Fundamental Interactions of Matter, Institute of Quantum Matter, South China Normal University, Guangzhou 510006, China*
[6]*Guangdong-Hong Kong Joint Laboratory of Quantum Matter, Guangdong Provincial Key Laboratory of Nuclear Science, Southern Nuclear Science Computing Center, South China Normal University, Guangzhou 510006, China*
[7]*University of Chinese Academy of Sciences, Beijing 100049, China.*
[8]*INPAC, Shanghai Key Laboratory for Particle Physics and Cosmology, Key Laboratory for Particle Astrophysics and Cosmology (MOE), School of Physics and Astronomy, Shanghai Jiao Tong University, Shanghai 200240, China*
[9]*Southern Center for Nuclear-Science Theory (SCNT), Institute of Modern Physics, Chinese Academy of Sciences, Huizhou 516000, Guangdong Province, China*
[10]*School of Fundamental Physics and Mathematical Sciences, Hangzhou Institute for Advanced Study, UCAS, Hangzhou 310024, China*
[11]*International Centre for Theoretical Physics Asia-Pacific, Beijing/Hangzhou 100049, China*

(Received 8 November 2023; accepted 3 January 2024; published 19 March 2024)

We present the light-flavor quark masses and low-energy constants using the $2+1$ flavor full-QCD ensembles with stout smeared-clover fermion action and Symanzik gauge action. Both the fermion and gauge actions are tadpole improved self-consistently. The simulations are performed on 11 ensembles at three lattice spacings $a \in [0.05, 0.11]$ fm, four spatial sizes $L \in [2.5, 5.1]$ fm, seven pion masses $m_\pi \in [135, 350]$ MeV, and several values of the strange quark mass. The quark mass is defined through the partially conserved axial current relation and renormalized to $\overline{\mathrm{MS}}(2\,\mathrm{GeV})$ through the intermediate regularization independent momentum subtraction scheme. The systematic uncertainty of using the symmetric momentum subtraction scheme is also included. Eventually, we predict $m_u = 2.45(22)(20)$ MeV, $m_d = 4.74(11)(09)$ MeV, and $m_s = 98.8(2.9)(4.7)$ MeV with the systematic uncertainties from lattice spacing determination, continuum extrapolation and renormalization constant included. We also obtain the chiral condensate $\Sigma^{1/3} = 268.6(3.6)(0.7)$ MeV and the pion decay constant $F = 86.6(7)(1.4)$ MeV in the $N_f = 2$ chiral limit, and the next-to-leading order low-energy constants $\ell_3 = 2.43(54)(05)$ and $\ell_4 = 4.322(75)(96)$.

DOI: 10.1103/PhysRevD.109.054507

*Corresponding author: liuming@impcas.ac.cn
†Corresponding author: pengsun@impcas.ac.cn
‡Corresponding author: ybyang@itp.ac.cn

I. INTRODUCTION

As fundamental parameters of the standard model which are not directly measurable in experiments, the mass of the lightest three flavors can only be determined accurately using lattice quantum chromodynamics (QCD). Lattice QCD offers a nonperturbative approach to solve QCD, the underlying theory of the strong interactions, but a set of

complete and accurate ensembles is essential to ensure reliable results.

Due to the infamous fermion doubling problem which prevents a straightforward discretization of the continuum Dirac fermion action, an accurate determination of the light quark masses is highly nontrivial. Since the widely used clover fermions suffer the additional chiral symmetry breaking which induces power divergence with loop corrections, most of the light quark mass determinations are made with either the staggered fermion (or its improved versions) [1–13] which suffers the mixing between four equivalent "tastes" of a given flavor, or Ginsburg-Wilson fermion actions like domain wall [14–18] or overlap [19] fermions which requires $\mathcal{O}(10\text{–}100)$ times more cost of computational resources than the clover fermions.

Thus a natural question is, whether it is possible for the clover fermion to reach a high accuracy determination of the light quark masses. In 2007, Ishikawa *et al.* [20] proposed an alternative approach to define light quark masses from the partially conserved axial current (PCAC) relation and renormalize it with tadpole improved one-loop matching. By utilizing the Schrödinger functional (SF) scheme [21], the PCAC quark mass can be renormalized nonperturbatively, and the calculation of the physical pion mass with a single lattice spacing $a = 0.09$ fm and $m_\pi L \sim 2$ gives $m_{u,d} = 3.12(24)(08)$ MeV [22–25] at $\overline{\text{MS}}(2\text{ GeV})$, which is 10% lower than the present lattice average value $m_{u,d} = 3.381(40)$ MeV [26] with large uncertainty.

A more systematic study using the SF scheme was conducted by the ALPHA Collaboration with multiple lattice spacing $a \in [0.05, 0.086]$ fm but relatively heavy quark masses $m_\pi \geq 200$ MeV, and their determination resulted in $m_{u,d} = 3.54(12)(9)$ MeV [27]. So far, the most precise determination of $m_{u,d} = 3.469(47)(48)$ [27,28] with clover fermion comes from the BMW Collaboration, which utilized multiple lattice spacings $a \in [0.05, 0.012]$ fm with the lightest pion mass $m_\pi = 131(2)$ MeV and renormalized the quark mass using the widely used regularization independent momentum subtraction (RI/MOM) scheme [29].

But the systematic uncertainty of using the RI/MOM scheme could be underestimated, as the RI/MOM scheme exhibits poor perturbative convergence for the scalar/pseudoscalar current, leading to sensitivity in the final result due to the estimate of the missing higher-order corrections. Thus, the symmetric momentum subtraction (SMOM) scheme [30,31] was proposed to suppress this uncertainty and has been employed in most recent quark mass determinations using chiral fermions. Nevertheless, a recent study [32] at multiple lattice spacings shows that using either the RI/MOM or SMOM intermediate scheme can result in the renormalized scalar current under $\overline{\text{MS}}$ scheme differing by 30% at $a \sim 0.1$ fm for the clover fermion.

Additionally, it is worth mentioning that the renormalized quark mass using the RI/MOM scheme with the twisted-mass fermion [33–35] is $m_{u,d} = 3.64(7)(6)$ MeV, which is approximately 5% higher than the results obtained with chiral fermions that predominantly use the SMOM scheme.

In this work, we conduct a detailed comparison of the renormalization constants (RCs) using the RI/MOM and SMOM schemes. It turns out that the sensitivity of the intermediate schemes can be suppressed to ∼5% level, which allows us to provide a relatively precise prediction of the quark mass. Based on the kaon masses with the QED effect subtracted, we also obtain the up, down, and strange quark masses separately, along with other related quantities. We expect that further improvement in the prediction accuracy can be achieved through calculations on more lattice spacings.

II. SIMULATION SETUP

The results in this work, are based on the $2 + 1$ flavor full-QCD ensembles using the tadpole-improved tree-level Symanzik (TITLS) gauge action and the tadpole-improved tree-level clover (TITLC) fermion action.

The TITLS gauge action, denoted as S_g, is defined in the following:

$$S_g = \frac{1}{N_c}\text{Re}\sum_{x,\mu<\nu}\text{Tr}\left[1-\hat{\beta}\left(\mathcal{P}^U_{\mu,\nu}(x)+\frac{c_1\mathcal{R}^U_{\mu,\nu}(x)}{1-8c_1^0}\right)\right], \quad (1)$$

where $N_c = 3$, and

$$\begin{aligned}\mathcal{P}^U_{\mu,\nu}(x) &= U_\mu(x)U_\nu(x+a\hat{\mu})U^\dagger_\mu(x+a\hat{\nu})U^\dagger_\nu(x),\\ \mathcal{R}^U_{\mu,\nu}(x) &= U_\mu(x)U_\mu(x+a\hat{\mu})U_\nu(x+2a\hat{\mu})\\ &\quad\times U^\dagger_\mu(x+a\hat{\mu}+a\hat{\nu})U^\dagger_\mu(x+a\hat{\nu})U^\dagger_\nu(x),\\ U_\mu(x) &= P\left[\exp\left(ig_0\int_x^{x+\hat{\mu}a}dyA_\mu(y)\right)\right],\end{aligned}$$

and $\hat{\beta} = (1-8c_1^0)\frac{6}{g_0^2u_0^4} \equiv 10/(g_0^2u_0^4)$ with $c_1^0 = -\frac{1}{12}$, $c_1 = \frac{c_1^0}{u_0^2}$, $u_0 = \langle\frac{\text{ReTr}\sum_{x,\mu<\nu}\mathcal{P}^U_{\mu\nu}(x)}{6N_c\tilde{V}}\rangle^{1/4}$ is the tadpole improvement factor, $\tilde{V} = \tilde{L}^3\times\tilde{T}$ is the dimensionless 4D volume of the lattice, and we use $\tilde{O}$ for the dimensionless value of any quantity O.

The TITLC fermion action uses 1-step stout smeared link V with smearing parameter $\rho = 0.125$,

$$\begin{aligned}S_q(m) &= \sum_{x,\mu=1,\ldots,4,\eta=\pm}\bar{\psi}(x)\sum\frac{1+\eta\gamma_\mu}{2}V_{\eta\mu}(x)\psi(x+\eta\hat{\mu}a)\\ &\quad+\sum_x\psi(x)[-(4+ma)\delta_{y,x}+c_{\text{sw}}\sigma^{\mu\nu}g_0F^V_{\mu\nu}]\psi(x),\end{aligned} \quad (2)$$

where $c_{\text{sw}} = \frac{1}{v_0^3}$ with $v_0 = \langle\frac{\text{ReTr}\sum_{x,\mu<\nu}\mathcal{P}^V_{\mu\nu}(x)}{6N_c\tilde{V}}\rangle^{1/4}$, and

TABLE I. Lattice size $\tilde{L}^3 \times \tilde{T}$, gauge coupling $\hat{\beta} = 10/(g^2 u_0^4)$, dimensionless bare quark mass parameters $\tilde{m}^{\mathrm{b}}_{l,s}$, renormalized quark masses $m^R_{l,s}$ and the corresponding pseudoscalar mass $m_{\pi,K}$, and the statistics information.

	C24P34	C24P29	C32P29	C32P23	C48P23	C48P14	F32P30	F48P30	F32P21	F48P21	H48P32
$\tilde{L}^3 \times \tilde{T}$	$24^3 \times 64$	$24^3 \times 72$	$32^3 \times 64$	$32^3 \times 64$	$48^3 \times 96$	$48^3 \times 96$	$32^3 \times 96$	$48^3 \times 96$	$32^3 \times 64$	$48^3 \times 96$	$48^3 \times 144$
$\hat{\beta}$				6.20					6.41		6.72
a (fm)				0.10530(18)					0.07746(18)		0.05187(26)
$\tilde{m}^b_l$	−0.2770	−0.2770	−0.2770	−0.2790	−0.2790	−0.2825	−0.2295	−0.2295	−0.2320	−0.2320	−0.1850
$\tilde{m}^b_s$	−0.2310	−0.2400	−0.2400	−0.2400	−0.2400	−0.2310	−0.2050	−0.2050	−0.2050	−0.2050	−0.1700
m^R_l (MeV)	22.90(19)	16.94(12)	17.35(11)	10.55(11)	10.27(10)	3.638(83)	18.54(12)	18.511(92)	8.58(16)	8.59(08)	19.42(05)
m^R_s (MeV)	111.41(16)	87.46(10)	88.16(10)	84.48(07)	84.79(04)	103.15(05)	93.23(11)	93.05(08)	89.75(10)	90.43(08)	95.61(04)
m_π (MeV)	341.1(1.8)	292.7(1.2)	292.4(1.1)	228.0(1.2)	225.6(0.9)	135.5(1.6)	303.2(1.3)	303.4(0.9)	210.9(2.2)	207.2(1.1)	317.2(0.9)
m_K (MeV)	582.7(1.6)	509.4(1.1)	509.0(1.1)	484.1(1.0)	484.1(1.3)	510.0(1.0)	524.6(1.8)	523.6(1.4)	492.0(1.7)	493.0(1.4)	536.1(3.0)
n_{cfg}	200	476	198	400	62	203	206	99	194	98	176
n_{src}	32	3	3	3	3	48	3	3	3	12	12

$$F^V_{\mu\nu} = \frac{i}{8a^2 g_0}(\mathcal{P}^V_{\mu,\nu} - \mathcal{P}^V_{\nu,\mu} + \mathcal{P}^V_{\nu,-\mu} - \mathcal{P}^V_{-\mu,\nu} + \mathcal{P}^V_{-\mu,-\nu} - \mathcal{P}^V_{-\nu,-\mu} + \mathcal{P}^V_{-\nu,\mu} - \mathcal{P}^V_{\mu,-\nu}). \quad (3)$$

The parameters utilized for the simulation, encompassing the lattice size ($\tilde{L}^3 \times \tilde{T}$), gauge coupling ($\hat{\beta}$), and the lattice spacing (a) determined through the gradient flow [36] with w_0 [37] using the Symanzik action, are outlined in Table I. The dimensionless bare degenerated light and strange quark mass ($\tilde{m}^{\mathrm{b}}_{l,s}$), renormalized quark masses ($m^R_{l,s}$) at $\overline{\mathrm{MS}}(2\,\mathrm{GeV})$, and the respective pion and kaon masses ($m_{\pi,K}$) are also included in the table. The details of the pseudoscalar meson mass and lattice spacing extraction can be found in Appendixes A 1 a and A 1 b. The impact of the mistuning effect of the tadpole improvement factors u_0 and v_0 can also be found there (Appendix A 1 c).

The ensemble set used in this work is designed to control the variables in the systematic uncertainty estimation. For example, the spatial size L of the C24P29, F32P30, and H48P32 ensembles are all within 1–2% of each other, and the unitary pion masses are also similar with a 10% difference. Thus, they are very suitable for investigating the discretization error of the hadron structure with nonzero given momentum. The pion mass and volume of C32P23 are close to those of F48P21 within 10%, and remaining differences can be further suppressed by interpolation with the other ensembles or by generating a new ensemble C36P21 using interpolated parameters. The other ensembles with larger dimensionless volume, such as F64P14 and/or H64P22, should also be helpful in achieving better control over the discretization error, and will be generated in the future.

For the clover fermion action, defining the renormalized quark mass m^R_q from the bare quark mass parameter $\tilde{m}^b_q$ can be subtle since the critical quark mass $\tilde{m}_{\mathrm{crti}}$ vanishing the pion mass is nonzero. A more practical solution defines it through the PCAC relation [20],

$$Z_A \partial_\mu A_\mu = 2 m^R_q Z_P P, \quad (4)$$

where $A_\mu = \bar{\psi}\gamma_5\gamma_\mu\psi$ and $P = \bar{\psi}\gamma_5\psi$. The PCAC quark mass m^{PC}_q is then defined through the pion-correlation functions,

$$m^{\mathrm{PC}}_q = \left.\frac{m_{\mathrm{PS}} \sum_{\vec{x}} \langle A_4(\vec{x}, t) P^\dagger(\vec{0}, 0)\rangle}{2\sum_{\vec{x}} \langle P(\vec{x}, t) P^\dagger(\vec{0}, 0)\rangle}\right|_{t\to\infty}, \quad (5)$$

where m_{PS} is the pseudoscalar meson mass. The renormalized quark mass is subsequently defined as $m^R_q = Z_A/Z_P m^{\mathrm{PC}}_q$.

In Fig. 1, we plot the dimensionless PCAC quark mass $\tilde{m}^{\mathrm{PC}}_q \equiv m^{\mathrm{PC}}_q a$ as a function of the dimensionless input bare quark mass parameters $\tilde{m}^b_q \equiv m^{\mathrm{b}}_q a$, at three lattice spacings with $m_\pi \sim 300$ MeV. The figure also includes linear fits using the following form:

$$\tilde{m}^{\mathrm{PC}}_q = k_m(\tilde{m}^b_q - \tilde{m}_{\mathrm{crti}}), \quad (6)$$

where $\tilde{m}_{\mathrm{crti}}$ corresponds to the critical pion mass that makes the pion mass and $\tilde{m}^{\mathrm{PC}}$ vanish. The parameter $k_m = 1 + \mathcal{O}(a^2, \alpha_s, a\alpha_s)$ approaches $1/Z_A$ determined by nonperturbative RI/MOM renormalization (due to the relation $Z_m Z_P = 1$) in the continuum limit, while it is affected by the $\mathcal{O}(a^2)$ discretization error and $\mathcal{O}(\alpha_s)$ loop effects at finite lattice spacing.

Unlike the hadron mass, the determination of physical quark mass on the lattice using discretized actions requires additional renormalization. The RCs defined under the $\overline{\mathrm{MS}}$ scheme, can only be obtained through regularization-independent (RI) schemes such as RI/MOM [29] or

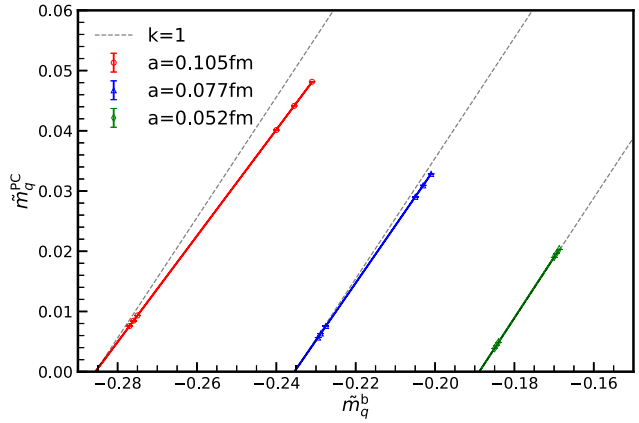

FIG. 1. The dimensionless PCAC quark mass $\tilde{m}_q^{\rm PC} = m_q^{\rm PC} a$ vs the bare quark mass $\tilde{m}_q^{\rm b} = m_q^{\rm b} a$ at three lattice spacings. The slope should approach 1 in the continuum limit. The data points correspond to six valence quark masses around the unitary light and strange quark masses in those ensembles.

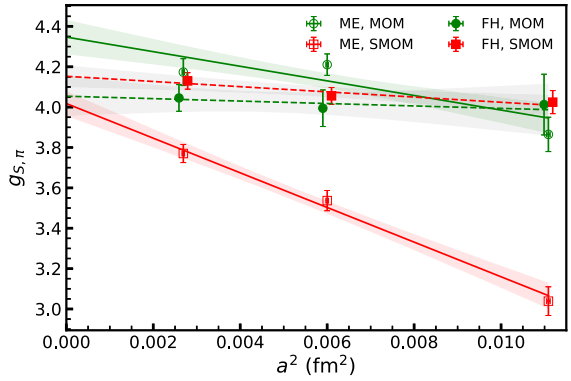

FIG. 2. Renormalized scalar matrix element $g_{S,\pi}$ with $m_\pi = 317$ MeV at three lattice spacing. $g_{S,\pi,\rm ME}$ used $Z_S^{\overline{\rm MS}(2\ {\rm GeV})}$, $g_{S,\pi,\rm FH}$ used $Z_P^{\overline{\rm MS}(2\ {\rm GeV})}$, through either the RI/MOM or SMOM scheme. The extrapolated values deviate by ∼7%.

SMOM [30,31]. These RCs should be independent of intermediate schemes.

For the overlap fermion action, which possesses strict chiral symmetry, the relations $Z_V = Z_A$ and $Z_P = Z_S = 1/Z_m$ are satisfied strictly. The scheme dependence of RI/MOM or SMOM can be ignored compared to other systematic uncertainties [38].

However, in the case of the clover fermion action, the ratio Z_A/Z_V can deviate from unity due to the additive chiral symmetry breaking effect generated by additional terms in the action, and it is sensitive to the choice of using RI/MOM or SMOM scheme. Based on the f_π at three lattice spacing with $m_\pi = 317$ MeV, the scheme sensitivity is approximately 1% after a linear a^2 continuum extrapolation, with the discretization error through RI/MOM being 25% smaller than that of SMOM.

For the chiral symmetry breaking effect between Z_S and Z_P, it is valuable to consider the scalar matrix element with the valence quark contribution only,

$$g_{S,\pi,\rm ME} = \langle \pi | S | \pi \rangle_{\rm val} / \langle \pi | \pi \rangle, \tag{7}$$

where $S = \bar{\psi}\psi$. We show the renormalized $g_{S,\pi,\rm ME}^{\overline{\rm MS}(2\ {\rm GeV})} = Z_S^{\overline{\rm MS}(2\ {\rm GeV})} g_{S,\pi}$ obtained from RI/MOM and SMOM schemes in Fig. 2, for $m_\pi = 317$ MeV at three different lattice spacings. It can be observed that the RI/MOM scheme exhibits a smaller discretization error than that of the SMOM scheme, and the continuum extrapolated values differ from each other by approximately 7.6(2.3)%.

Using the Feynman-Hellman theorem, one can also extract $g_{S,\pi}$ from the quark mass dependence of m_π, as

$$g_{S,\pi,\rm FH} = \frac{1}{2}\frac{\partial m_\pi(m_q)}{\partial m_q} \simeq \frac{m_\pi}{4 m_q} + \mathcal{O}(m_q, a^2), \tag{8}$$

where the factor $\frac{1}{2}$ in front of $\frac{\partial m_\pi(m_q)}{\partial m_q}$ is used to average the contribution from two propagators in the pion correlator. Using the renormalized quark mass $m_q^{\overline{\rm MS}(2\ {\rm GeV})}$ extracted with the RI/MOM or SMOM scheme, $g_{S,\pi,\rm FH}^{\overline{\rm MS}(2\ {\rm GeV})}$ (filled green dots for MOM and red boxes for SMOM) are in the range of 3.9 to 4.2 and then slightly smaller than the linear a^2 extrapolated value $g_{S,\pi,\rm ME} = 4.35(9)$ (green band) using the RI/MOM scheme but consistent with the SMOM value 4.02(6) (red band). Even more, $g_{S,\pi,\rm FH}$ is consistent with the $g_{S,\pi,\rm ME}$ using the RI/MOM scheme at each lattice spacing within two sigma, but have significant difference from the $g_{S,\pi,\rm ME}$ using the SMOM scheme. Thus, the deviation between the $g_{S,\pi,\rm FH}$ and $g_{S,\pi,\rm ME}$ using the RI/MOM scheme would be only a systematic uncertainty due to the linear a^2 extrapolation. Thus the renormalized g_S shall have about 7% systematic uncertainty with present data, and more reliable continuum extrapolation with data at more lattice spacing is essential to obtain accurate prediction on g_S.

The renormalization constants for various quark bilinear operators are detailed in Appendix A 2, along with a discussion on the discretization error from different renormalization methods of quark field and mass.

III. RESULTS

Using the lattice spacing shown in Table I, we find that the unitary pion mass on the ensemble C48P14 at $a = 0.1053(2)$ fm is 135.5(1.6) MeV, which perfectly agrees with the physical neutral pion mass m_{π^0} of 134.98 MeV within 1% statistical uncertainty. The charged pion mass $m_{\pi^\pm}$139.57 MeV receives the QED correction 4.53(6) MeV [39] and then the subtracted pure QCD $m_{\pi^\pm}$ is consistent with that of m_{π^0} within the uncertainty.

The corresponding renormalized light quark mass and pion decay constants can also be determined as

$$m_l^{\overline{\rm MS}(2\ {\rm GeV})}(a = 0.105\ {\rm fm}) = 3.64(8)(11)\ {\rm MeV},$$
$$f_\pi(a = 0.105\ {\rm fm}) = 121.9(5)\ {\rm MeV}, \quad (9)$$

where the second uncertainty of m_q comes from that of the renormalization constant. Based on the continuum extrapolation with a 317 MeV pion mass, the pion decay constant can change by approximately 7%, and then agree with the present PDG value 130.4(0.2) MeV [40] after the continuum extrapolation.

In order to process this continuum extrapolation systematically, we calculate the quark propagators with unitary light quark mass and also two partially quenched quark masses with the constraint $m_\pi L > 3.5$, on each of the 11 ensembles. Then we use the next-to-leading order (NLO) partially quenched χPT form [41] to describe the pion masses and decay constants with different valence and sea quark masses, in addition to extra parameters $c_{m/f,a/l}$ for the finite-lattice spacing/volume corrections.

Since the statistics on each ensemble are different, we perform 4000 bootstrap re-samplings on each ensemble and conduct the correlated global fit based on these bootstrap samples. In such a strategy, the correlation between different data points in the same ensemble is included automatically, and that between different ensembles vanishes within the statistical uncertainty of the re-sampling. The lattice spacing and renormalization constants are sampled for each bootstrap sample using a Gaussian distribution with their uncertainties as the width of the distribution.

To illustrate the lattice spacing dependence and the unitary quark mass dependence, we subtract the partially quenching effect using bootstrap samples of the fit parameters from the original data points, and show the ratio $(m_\pi)^2/m_q^{\overline{\rm MS}(2\ {\rm GeV})}$ (upper panel) and also f_π (lower panel) at different quark masses m_q in the Fig. 3. The corrected data points at different lattice spacings use different symbols: red crosses for $a = 0.105$ fm, blue triangles for $a = 0.077$ fm, and filled green dots for $a = 0.052$ fm. The bands with similar color represent the fitted band at the corresponding lattice spacing, and the gray band shows the final prediction in the continuum and infinite volume limit. It is observed that the continuum extrapolation pushes f_π to be obviously higher, while the impact on the (m_π^2/m_q) ratio and, consequently, m_q is much weaker.

The m_π and f_π with unitary valence and sea quark masses have the following parametrization,

$$m_\pi^2 = \Lambda_\chi^2 2y\left[1 + y\left(\ln\frac{2y\Lambda_\chi^2}{m_{\pi,{\rm phys}}^2} - \ell_3\right) + \mathcal{O}(y^2)\right], \quad (10)$$

$$F_\pi = F\left[1 - 2y\left(\ln\frac{2y\Lambda_\chi^2}{m_{\pi,{\rm phys}}^2} - \ell_4\right) + \mathcal{O}(y^2)\right], \quad (11)$$

where $\Lambda_\chi = 4\pi F$, $y = \frac{\Sigma m_l}{F^2\Lambda_\chi^2}$. Σ, F, and $\ell_{3,4}$ are low-energy constants. Our determination of those constants are also collected in Table II, consistent with the current $N_f = 2+1$ FLAG average but have smaller uncertainties except F.

In this work, we use the $m_{K^\pm}$ and m_{K^0} with the constraint $m_u^{\rm phys} + m_d^{\rm phys} = 2m_l^{\rm phys}$, to determine the up, down, and strange quark masses $m_{u,d,s}$. The QED correction on the kaon mass is subtracted based on the literature [34] under the renormalization scheme $m_{q,{\rm QCD+QED}}^{\overline{\rm MS}}(2\ {\rm GeV}) = m_{q,{\rm QCD}}^{\overline{\rm MS}}(2\ {\rm GeV})$. On each ensemble, we calculate the strange quark propagators with a unitary strange quark mass $m_s^{\rm v} = m_s^{\rm s}$, and also two partially quenched quark masses $m_s^{\rm v} \sim 100$ MeV. We construct the kaon correlation functions with three strange quark masses and three light quark masses used in the pion case. The 3×3 partially quenched kaon masses on all the ensembles are fitted with the following form proposed in a recent work [35]:

TABLE II. Summary of our determination on quark masses at $\overline{\rm MS}(2\ {\rm GeV})$ and the other quantities, through the intermediate RI/MOM or SMOM schemes, with comparison with FLAG [26] and/or PDG [40]. The difference between two schemes is considered as systematic uncertainty in the combined determination.

	m_l (MeV)	m_u (MeV)	m_d (MeV)	m_s (MeV)	$\Sigma^{1/3}$ (MeV)	m_s/m_l	m_u/m_d
RI/MOM	3.60(11)	2.45(22)	4.74(11)	98.8(2.9)	268.6(3.6)	27.47(30)	0.519(51)
SMOM	3.45(05)	2.25(10)	4.65(08)	94.1(1.2)	269.3(1.8)	27.28(22)	0.485(26)
Combined	3.60(11)(15)	2.45(22)(20)	4.74(11)(09)	98.8(2.9)(4.7)	268.6(3.6)(0.7)	27.47(30)(13)	0.519(51)(34)
FLAG/PDG	3.381(40)	2.27(09)	4.67(09)	92.2(1.0)	272(5)	27.42(12)	0.485(19)

	F (MeV)	F_π/F	f_π (MeV)	$f_{K^\pm}$ (MeV)	$f_{K^\pm}/f_\pi$	ℓ_3	ℓ_4
RI/MOM	86.6(7)	1.0675(19)	130.7(0.9)	155.6(0.8)	1.1907(76)	2.43(54)	4.322(75)
SMOM	85.1(6)	1.0683(15)	128.6(0.8)	152.9(0.7)	1.1890(74)	2.49(23)	4.226(48)
Combined	86.6(7)(1.4)	1.0675(19)(08)	130.7(0.9)(2.1)	155.6(0.8)(2.7)	1.1907(76)(03)	2.43(54)(05)	4.322(75)(96)
FLAG/PDG	86.8(6)	1.062(7)	130.2(0.8)	155.7(0.7)	1.1917(37)	3.07(64)	4.02(45)

$$m_K^2(m_l^{\rm v}, m_l^{\rm s}, m_s^{\rm v}, m_s^{\rm s}, a) = (b_s^{\rm v} m_s^{\rm v} + b_s^{\rm s} m_s^{\rm s} + b_l^{\rm v} m_l^{\rm v} + b_l^{\rm s} m_l^{\rm s}) \times [1 + c_l^K m_l^{\rm v} + c_m^K a^2 + c_L^K \exp(-m_\pi L)]. \quad (12)$$

The global fit result is showed in Table XI. Based on the fit of m_K^2, the total strange quark mass dependence $b_s^{\rm v} + b_s^{\rm s} = 2.37(08)$ is consistent with the leading-order light quark mass dependence $b_l^{\rm v} + b_l^{\rm s} = 2.59(95)$, and the coefficient of the nonlinear quark mass dependence $c_l^K = 1.2(3.3) \times \text{GeV}^{-1}$ can not be determined based on current statistics.

In Fig. 4, we show the corrected kaon mass $m_K^{\rm cr}$ and decay constant $f_K^{\rm cr}$ with the light quark mass m_l corrected to its physical value $m_l^{\rm phys}$. The finite volume and partially quenched effects are also subtracted. We can found that f_K also exhibits a strong lattice spacing dependence, similar to the f_π case, while the kaon mass is insensitive to the lattice spacing.

As illustrated in Figs. 3 and 4, all the global fits of the pseudoscalar meson mass and decay constant provide reasonable χ^2/d.o.f. More information on the global fit can be found in Appendix A 3.

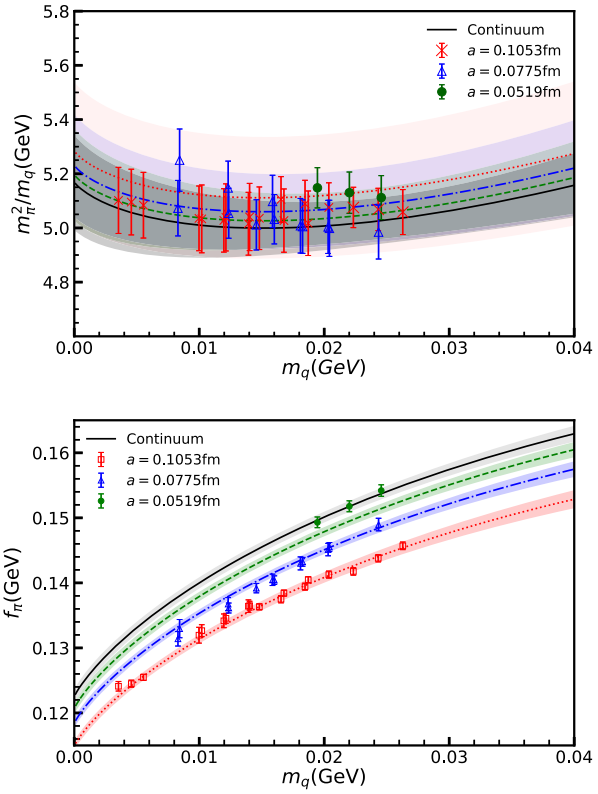

FIG. 3. The corrected unitary $(m_\pi^{\rm uni})^2/m_q$ and the decay constant $f_\pi^{\rm uni}$ varies with the quark mass, at three lattice spacing (colored data points and corresponding bands with dashed line for 0.0519 fm, dash-dotted line for 0.0775 fm, and dotted line for 0.1053 fm) and also continuum (gray band).

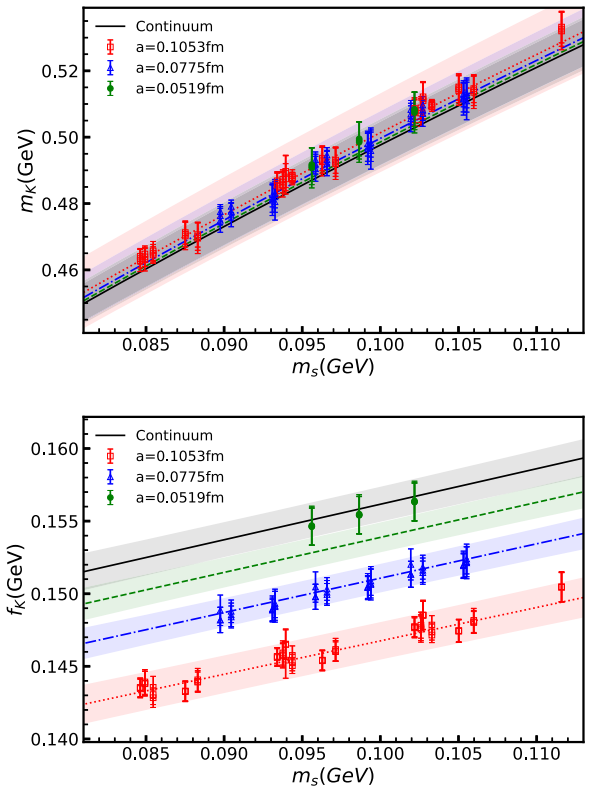

FIG. 4. The corrected kaon mass $m_K^{\rm cr}$ and the decay constant $f_K^{\rm cr}$ with the physical light quark mass $m_l^{\rm phys}$, varies with the strange quark mass at three lattice spacing (colored data points and bands) and also continuum (gray band).

The physical quark masses $m_{u,d,s}$ and also corresponding $f_{\pi,K}$ using $m_l^{\rm phys}$ and intermediate RI/MOM scheme, are collected in Table II. In addition, Table II shows the global fit results using the $Z_{A,P}$ through the SMOM scheme for comparison. As we can see from the continuum extrapolation tests using a 317 MeV pion mass, the SMOM scheme yields quark masses that are 3–4% lower and decay constants that are ∼2% lower compared to the RI/MOM scheme. However, the ratio of the quark masses or decay constants remains unchanged within the uncertainty as the renormalization constants are canceled.

Therefore, we consider the result using the RI/MOM scheme as the central value due to its smaller discretization error, and treat the difference between the results obtained using the two schemes as systematic uncertainties. Such a systematic uncertainty can also be considered as an estimate of the residual discretiation error, as the correct continuum limit should be independent of the intermediate renormalization scheme. All our determinations are consistent with the present lattice averages [26] and/or PDG [40] within $1-2\sigma$.

IV. SUMMARY

In this work, we determine the up, down, and strange quark masses, along with several low-energy constants,

using the $2+1$ flavor full-QCD ensembles with tadpole-improved clover and Symanzik actions. The major results are summarized in Table II.

Similar to one of the most precise works [28] with the clover fermion, we have skipped the axial current improvement [42] since the improvement coefficient itself strongly depends on the lattice spacing a and bring the improvement term to be consistent with an $\mathcal{O}(a^2)$ correction. As evidence, both f_π and m_q show good consistency with a simple linear a^2 lattice spacing dependence. Then assigning $c_A \sim 0.05a/(0.105\ \mathrm{fm})$ in the improved axial vector current $A_\mu^{\mathrm{imp}} = A_\mu + c_A a\partial_\mu P$ [42] can eliminate the discretization error in $f_{\pi,K}$, however, this error will be transferred to the quark mass. Thus, simulations at more lattice spacings would be a more systematic solution to enhance the accuracy of our predictions in the continuum than the axial current improvement.

On the other hand, the additive chiral symmetry breaking makes the renormalization of the quark mass to be highly nontrivial. Our study suggests that the Z_S and Z_P obtained through the SMOM scheme are closer than those through the RI/MOM scheme, while the latter one can make the discretization error of both the $m_q^R = Z_A/Z_P m_q^{\mathrm{PC}}$ and $g_S^R = Z_S g_S$ to be smaller. Our final prediction of the quark masses are 5.6(2.8)% higher than the current $(2+1)$-flavor lattice averages but consistent with the previous $(2+1)$- and $(2+1+1)$-flavor results using the RI/MOM scheme. At the same time, the RI/MOM scheme can also cause the Feynman-Hellman theorem $g_{S,\pi} \simeq \frac{m_\pi}{4m_q}$ to be violated by 7 (3)% after the linear $\mathcal{O}(a^2)$ continuum extrapolation.

Using the SMOM scheme can eliminate the violation and bring the quark mass prediction closer to the current $(2+1)$-flavor lattice average. However, the SMOM scheme introduces larger discretization errors for all the renormalized quantities we investigated and causes the decay constants $f_{\pi,K}$ to be 2–3% smaller than the physical values after the linear $\mathcal{O}(a^2)$ continuum extrapolation.

The above observations indicate that renormalization is a significant issue that requires careful investigation, and conducting similar calculations using chiral fermions would be essential to gain a better understanding of these violations. At the same time, nonperturbative renormalization should remove all the $\mathcal{O}(\alpha_s)$ effects, but not all the cross terms like the residual $\mathcal{O}(a\alpha_s)$ effect of the clover action, which can cause the $\mathcal{O}(a^2)$ continuum extrapolation to fail. Thus, we consider the difference between the results obtained by the two schemes as systematic uncertainties in our final determination of the aforementioned quantities, which are larger than the statistical uncertainties in various cases. We anticipate that additional research utilizing ensembles with a greater number of lattice spacings can encompass both the $\mathcal{O}(a^2)$ and $\mathcal{O}(a\alpha_s)$ terms in the continuum extrapolation, resulting in a more dependable and uniform continuum limit.

It is worth mentioning that in Ref. [28], the trace-subtraction trick $\bar{S} = S - \frac{1}{4}\mathrm{Tr}[S]$ is applied into renormalization procedure, and the quark mass is renormalized at RI/MOM 2 GeV, followed by perturbative matching at a much higher scale. This approach is crucial in suppressing their truncation error to the sub-percent level. However, in our case, it appears to be inefficient due to significant nonperturbative effects observed at 2 GeV. We plan to conduct a more systematic investigation once the CLQCD ensembles at more lattice spacings are generated.

ACKNOWLEDGMENTS

We thank Ying Chen, Hengtong Ding, Xu Feng, Chuan Liu, Zhaofeng Liu, Qi-An Zhang, and the other CLQCD members for valuable comments and suggestions. The calculations were performed using the Chroma software suite [43] with QUDA [44–46] through HIP programming model [47]. The numerical calculation were carried out on the ORISE Supercomputer, HPC Cluster of ITP-CAS, the Southern Nuclear Science Computing Center (SNSC), the Siyuan-1 cluster supported by the Center for High Performance Computing at Shanghai Jiao Tong University, and Advanced Computing East China Subcenter. This work is supported in part by NSFC Grants No. 1229060, No. 1229062, No. 12293061, No. 12293065, and No. 12047503, No. 12125503, No. 12335003, No. 12293060, and No. 12175279, the science and education integration young faculty project of University of Chinese Academy of Sciences, the Strategic Priority Research Program of Chinese Academy of Sciences, Grants No. XDB34030303 and No. YSBR-101, and also NSFC-DFG joint grant under Grants No. 12061131006 and No. SCHA 458/22, Guangdong Major Project of Basic and Applied Basic Research No. 2020B0301030008. The numerical calculations in this paper have been done on the supercomputing system in the Dongjiang Yuan Intelligent Computing Center.

APPENDIX

1. Simulation details

This section is organized as follows. The dimensionless joint fit on the pseudoscalar meson mass, its decay constant, and the corresponding PCAC quark mass will be discussed in Appendix A 1 a. Based on the determination of an uniform lattice spacing at given $\hat{\beta}$ detailed in Appendix A 1 b, the mistuning effect of the tadpole improvement factors is not always negligible and will be addressed in Appendix A 1 c.

a. Dimensionless joint fit

We construct two kinds of the two-point functions for the meson states:

$$C^{\Gamma\Gamma'}_{2,wp}(t;m_q) = \sum_{\vec{x}} \langle \mathrm{Tr}[S^{\dagger}_C(\vec{x}, y_0+t; y_0; m_q)\gamma_5\Gamma \times S_C(\vec{x}, y_0+t; y_0; m_q)\Gamma'\gamma_5]\rangle / L^3, \quad \text{(A1)}$$

$$C^{\Gamma\Gamma'}_{2,ww}(t;m_q) = \sum_{\vec{x},\vec{z}} \langle \mathrm{Tr}[S^{\dagger}_C(\vec{x}, y_0+t; y_0; m_q)\gamma_5\Gamma \times S_C(\vec{z}, y_0+t; y_0; m_q)\Gamma'\gamma_5]\rangle / L^3, \quad \text{(A2)}$$

where C_2 is independent of the source time slice y_0 after taking expectation value, the Coulomb gauge fixed-wall source propagator is defined as

$$S_C(x; y_0; m_q) = \sum_{\vec{y}} S(x; \vec{y}, y_0; m_q, U_C), \quad \text{(A3)}$$

$S(x; y; m_q, U) \equiv \psi(x; m_q, U)\bar{\psi}(y; m_q, U)$ is the quark propagator of the quark field ψ with bare quark mass m_q on a given gauge configuration U, and U_C is the Coulomb gauge fixed configuration satisfying the gauge fixing condition $\mathrm{Im}[\sum_{i=1,2,3}(U_C(x) - U_C(x - a\hat{n}_i))] = 0$.

For the clover fermion action, the PCAC quark mass m_q is then defined through the pion correlation functions [20],

$$m^{\mathrm{PC}}_q = \left. \frac{m_{\mathrm{PS}} \sum_{\vec{x}} \langle A_4(\vec{x}, t) P^{\dagger}(\vec{0}, 0)\rangle}{2\sum_{\vec{x}} \langle P(\vec{x}, t) P^{\dagger}(\vec{0}, 0)\rangle} \right|_{t\to\infty}. \quad \text{(A4)}$$

The renormalized quark mass is subsequently defined as $m^R_q = Z_A/Z_P m^{\mathrm{PC}}_q$.

Through a joint fit ($\tilde{O}$ is the dimensionless value of any quantity O),

$$\left. \frac{\tilde{C}^{\mathcal{A}_4\mathcal{P}}_{2,wp}(\tilde{t}-1) - \tilde{C}^{\mathcal{A}_4\mathcal{P}}_{2,wp}(\tilde{t}+1)}{4\tilde{C}^{\mathcal{P}\mathcal{P}}_{2,wp}(\tilde{t})} \right|_{0\ll\tilde{t}\ll\tilde{T}} = \frac{\mathrm{Sinh}(\tilde{m}_{\mathrm{PS}})}{\tilde{m}_{\mathrm{PS}}} \tilde{m}^{\mathrm{PC}}_q, \quad \text{(A5)}$$

$$\left. \sqrt{\frac{\tilde{C}^{\mathcal{P}\mathcal{P}}_{2,wp}(\tilde{t})}{\tilde{C}^{\mathcal{P}\mathcal{P}}_{2,ww}(\tilde{t})}} \right|_{0\ll\tilde{t}\ll\tilde{T}} = \frac{\tilde{m}^2_{\mathrm{PS}}}{2\tilde{m}^{\mathrm{PC}}_q \sqrt{Z_{wp}}} \tilde{f}_{\mathrm{PS}}, \quad \text{(A6)}$$

$$\tilde{C}^{\mathcal{P}\mathcal{P}}_{2,wp}(\tilde{t})|_{0\ll\tilde{t}\ll\tilde{T}} = \frac{Z_{wp}}{2\tilde{m}_{\mathrm{PS}}} (e^{-\tilde{m}_{\mathrm{PS}}\tilde{t}} + e^{-\tilde{m}_{\mathrm{PS}}(\tilde{T}-\tilde{t})}), \quad \text{(A7)}$$

the PCAC quark mass $\tilde{m}^{\mathrm{PC}}_q$, pseudoscalar mass

$$\tilde{m}_{\mathrm{PS}} = \mathrm{Cosh}^{-1} \left. \frac{\tilde{C}^{\mathcal{P}\mathcal{P}}_{2,wp}(\tilde{t}-1) + \tilde{C}^{\mathcal{P}\mathcal{P}}_{2,wp}(\tilde{t}+1)}{2\tilde{C}^{\mathcal{P}\mathcal{P}}_{2,wp}(\tilde{t})} \right|_{0\ll\tilde{t}\ll\tilde{T}}, \quad \text{(A8)}$$

and decay constant $\tilde{f}_{\mathrm{PS}}$ are extracted as fit parameters, alongside an additional unphysical fit parameter Z_{wp} for the Coulomb gauge-fixed wall source.

In Fig. 5, we shown the joint fit result of the unitary light quark on the physical point ensemble C48P14. To suppress the statistical uncertainty, we repeated the calculation on $n_{\mathrm{src}} = 48$ of 96 times slides on $n_{\mathrm{cfg}} = 203$ configurations. The values of n_{src} and n_{cfg} of the other ensembles can be found in Table. I. The ratios (red data points) defined in Eq. (A5) for $\tilde{m}_q$ are consistent with a constant in the region of $\tilde{t} > 10$, as shown in the top left panel. The situation is similar for $\tilde{f}_{\mathrm{PS}}$ (top right panel) and also $\tilde{m}_{\mathrm{PS}}$ (bottom left panel). Since the statistics on C48P14 are limited, we performed a joint uncorrelated fit in the range $\tilde{t} \in [10, 40]$ for Eqs. (A5)–(A7) and used bootstrap resampling to estimate the uncertainty, represented by the gray band in the figure. We can see that the fit agrees very well with the data points, and the uncertainties of the fitted bands are comparable to the original data. Thus, it is unlikely that the uncertainty has been underestimated by the uncorrelated fit.

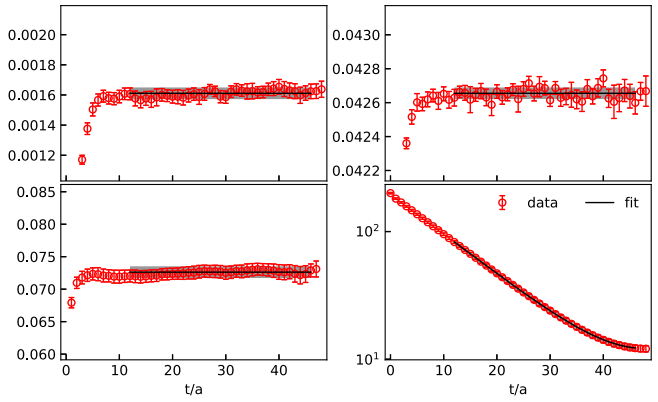

FIG. 5. The ratios for $\tilde{m}_q$ (left top), $\tilde{f}_{\mathrm{PS}}$ (right top), $\tilde{m}_{\mathrm{PS}}$ (left bottom) defined in Eqs. (A5)–(A8), and the correlator $\tilde{C}^{\mathcal{P}\mathcal{P}}_{2,wp}$ (right bottom) as functions of $\tilde{t}$, for the physical light quark mass at the coarsest lattice spacing. The joint-fit results are shown on the plots as gray bands.

The strange quark mass case on the ensemble C48P14 is shown in Fig. 6. Since the statistical uncertainty decreases with with a heavier quark mass, we only repeated the calculation on three time slides for each configuration,

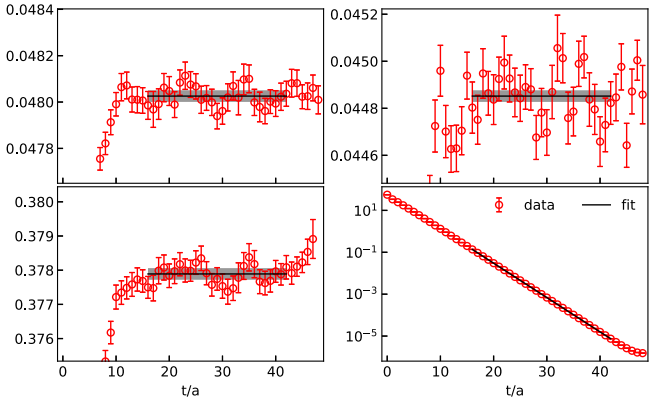

FIG. 6. Similar to Fig. 5 but for the strange quark mass and fewer sources ($n_{\mathrm{src}} = 3$).

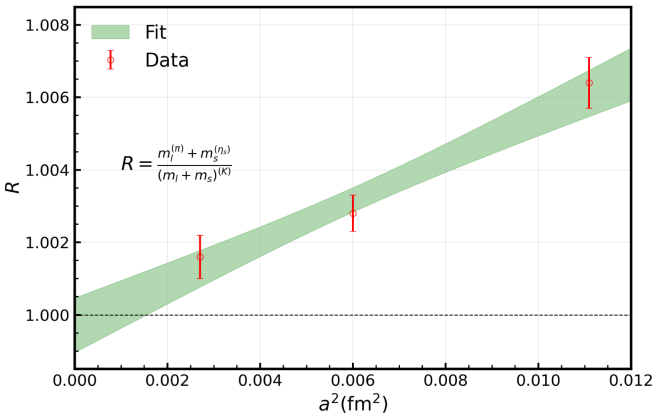

FIG. 7. The ratio of the PCAC quark mass determined from the quarkoinum (pion and η_s), and also kaon. Two definitions are consistent upto $\mathcal{O}(a^2)$ correction.

resulting in more noticeable fluctuations compared to the light quark case.

Through the above fit, we can extract the light and strange quark masses through the pion and η_s correlators, respectively,

$$\partial_\mu(\bar{l}\gamma_5\gamma_\mu l) = 2m_l^{\mathrm{PC}}\bar{l}\gamma_5 l, \qquad \partial_\mu(\bar{s}\gamma_5\gamma_\mu s) = 2m_s^{\mathrm{PC}}\bar{s}\gamma_5 l. \tag{A9}$$

Alternatively, the sum of the light and strange quark masses can also be extracted from the kaon correlator,

$$\partial_\mu(\bar{s}\gamma_5\gamma_\mu l) = (m_l^{\mathrm{PC}} + m_s^{\mathrm{PC}})\bar{s}\gamma_5 l. \tag{A10}$$

Thus, we should verify two extraction provide consistent result, at least in the continuum. Figure 7 shows the ratio of these two determinations of $m_l + m_s$ at three lattice spacings, with $m_\pi \sim 300$ MeV and $m_{\eta_s} \sim 700$ MeV for better signals. Two determinations deviate from each other by approximately 0.6% at the coarsest lattice spacing but are consistent within the statistical uncertainty of 0.1% after a linear a^2 extrapolation to the continuum limit.

At three lattice spacings with $m_\pi \sim 300$ MeV, we fit the dimensionless PCAC quark mass $\tilde{m}_q^{\mathrm{PC}} = m_q^{\mathrm{PC}} a$ with the following form:

$$\tilde{m}^{\mathrm{PC}} = k_m(\tilde{m}^b - \tilde{m}_{\mathrm{crti}}), \tag{A11}$$

where $\tilde{m}_q^b = m_q^{\mathrm{b}} a$ is the original input quark mass parameters, and $\tilde{m}_{\mathrm{crti}}$ corresponds to the critical pion mass that makes the pion mass and $\tilde{m}^{\mathrm{PC}}$ vanish. The parameter $k_m = 1 + \mathcal{O}(a^2, \alpha_s, a\alpha_s)$ approaches $1/Z_A$ determined by nonperturbative RI/MOM renormalization (due to the relation $Z_m Z_P = 1$) in the continuum limit, while it is affected by the $\mathcal{O}(a^2)$ discretization error and $\mathcal{O}(\alpha_s)$ loop effects at finite lattice spacing.

Based on the numerical results listed in Table III, we observe that $\tilde{m}_{\mathrm{crti}}$ remains negative even after a naive $\mathcal{O}(a) + \mathcal{O}(a^2)$ extrapolation to the continuum, with a value of -0.0865. Therefore, it is crucial to include the $\mathcal{O}((\alpha_s^b)^2)$ term, where $\alpha_s^b = \frac{g_0^2}{4\pi} = \frac{10}{4\pi\beta u_0^4}$, in the continuum extrapolation to ensure that $\tilde{m}_{\mathrm{crti}} \xrightarrow[a\to 0]{} 0$, as predicted by lattice perturbative theory.

TABLE III. The bare coupling α_s^{b}, critical quark mass $\tilde{m}_{\mathrm{crti}}$, and slope k_m at three lattice spacing a and $m_\pi \sim 300$ MeV.

a (fm)	0.105	0.077	0.052
$\alpha_s^{\mathrm{b}}(a)$	0.2397	0.2234	0.2035
$\tilde{m}_{\mathrm{crti}}$	−0.28560(4)	−0.23545(3)	−0.18885(1)
k_m	0.881(1)	0.953(1)	1.009(1)

On the other hand, the discrepancy between k_m and 1 diminishes as the lattice spacing becomes smaller. We will discuss this further in the following section on renormalization.

b. Lattice spacing determination

Figure 8 illustrates the lattice spacing determined by the gradient flow [36] with w_0 [37] at three bare couplings $\hat{\beta}$ and $m_\pi \sim 300$ MeV, using different gauge action improvement coefficient c_1 in the flow; $c_1 = -0.331$ (Iwasaki action), -0.2 and $-1/(12u_0^2)$ for interpolation, $-1/12$ (Symanzik action), and 0 (Wilson action). The c_1 dependence becomes weaker at smaller lattice spacings, indicating that it is a discretization effect. As the tadpole improvement factor approaches 1 with increasing gradient flow t, implementing tadpole improvement for the action used by the flow only affects the small flow time region and is unnecessary. Thus, we consistently use the standard $c_1 = -1/12$ in the gradient flow to match the gauge action employed in HMC and mitigate the discretization error.

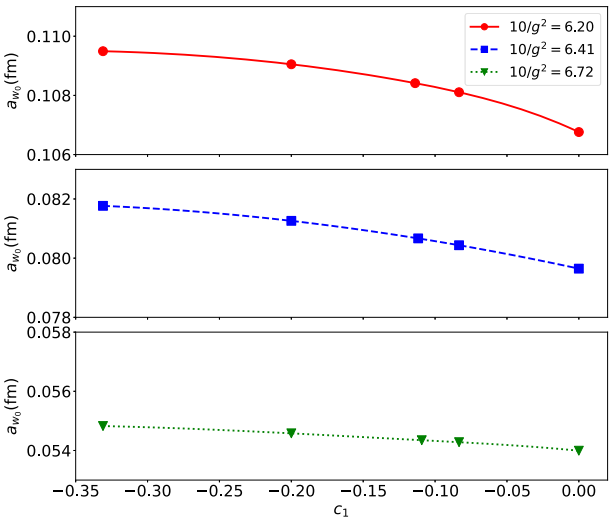

FIG. 8. The lattice spacings determined by w_0 with different gauge action improvement factor c_1.

TABLE IV. a_{w_0} on different ensembles and the fitted values through the functional form in Eq. (A12).

	a_{w_0}	$a_{w_0}^{\text{fit}}$	Fit parameters	
C24P34	0.11198(17)	0.11202(16)	$a(6.20)$	0.10530(18)
C24P29	0.10811(15)	0.10834(09)	$a(6.41)$	0.07746(18)
C32P29	0.10858(11)	0.10836(06)	$a(6.72)$	0.05187(26)
C32P23	0.10637(13)	0.10637(06)	c_l	0.507(18)
C48P23	0.10631(06)	0.10635(05)	c_s	0.110(23)
C48P14	0.10583(07)	0.10582(06)	c_L	0.001(09)
F32P30	0.08044(10)	0.08044(08)	c_{u_0}	−408(125)
F48P30	0.08017(05)	0.08017(05)	c_{v_0}	379(110)
F32P21	0.07758(16)	0.07757(15)		
F48P21	0.07810(07)	0.07809(06)		
H48P32	0.05430(11)	0.05430(11)		

Using the FLAG average value of the gradient flow scale, $w_0 = 0.1736(9)$ fm [26], the lattice spacing a_{w_0} for each ensemble is determined using the Symanzik flow and summarized in Table IV. It is evident that a_{w_0} primarily depends on the gauge coupling $\hat{\beta}$, while the quark mass also exhibits significant effects, as indicated by the precise a_{w_0} results with a statistical uncertainty of approximately 0.1%. Empirically, a_{w_0} can be described by the following parametrization, yielding a χ^2/d.o.f. of 2.2 (with a corresponding p-value of 0.09, still larger than the standard lower bound of 0.05):

$$\begin{aligned} &a_{w_0}(\hat{\beta}, \tilde{m}_\pi, \tilde{m}_{\eta_s}, \delta u_0, \delta v_0) \\ &= a(\hat{\beta})\left[1 + c_l\left(\frac{\tilde{m}_\pi^2}{a(\hat{\beta})^2} - m_{\pi,\text{phys}}^2\right)\right. \\ &\quad + c_s\left(\frac{\tilde{m}_{\eta_s}^2}{a(\hat{\beta})^2} - m_{\eta_s,\text{phys}}^2\right) + c_L e^{-\tilde{m}_\pi \tilde{L}} \\ &\quad \left. + c_{u_0}(u_0 - u_0^I) + c_{v_0}(v_0 - v_0^I)\right], \end{aligned} \tag{A12}$$

where, $m_{\pi,\text{phys}} = 134.98$ MeV [40] represents the physical pion mass without QED correction, and $m_{\eta_s,\text{phys}} = 689.63(18)$ MeV [48] corresponds to the pseudoscalar meson mass of the strange quark with only connected insertions. The tadpole improvement factors used in the actions are denoted as u_0^I and v_0^I, while u_0 and v_0 are tadpole improvement factors obtained from the generated configurations. The lattice spacing $a(\beta)$ with physical quark masses at each β, along with the other fitting parameters c_{l,s,L,u_0,v_0} are also provided in Table IV.

We observe that the volume dependence is consistent with zero, but there is still a nonvanishing mismatch effect ($u_0^I \neq u_0$ and $v_0^I \neq v_0$) in the tadpole improvement factors, like what be showed in Table V. It is also interesting to note that the dependence of a_{w_0} on the strange quark mass is weaker compared to that of the light quark mass by a factor of approximately 4, instead of 2 from two light flavors.

c. Mismatch effect of the tadpole improvement factors

As shown in Table IV, the mismatch effect of the tadpole improvement factors can have a nonzero impact on the determination of a_{w_0} through the gradient flow. Both u_0 and v_0 represent vacuum expectation values and cannot be accurately determined before generating gauge configurations using the realistic hybrid Monte Carlo (HMC) production. Therefore, for each ensemble, we initiate the HMC with an initial guess for u_0 and v_0, measure their values on each trajectory until they stabilize, and subsequently restart the HMC production with the updated values of u_0 and v_0. After several iterations, the input values u_0^{I} and v_0^{I} become consistent with u_0 and v_0, as measured from the configurations, at a level of approximately 0.002%, resulting in an effect of around 0.6% on the lattice spacing. The only exception is the test ensemble C24P34, which exhibits a larger deviation in both u_0 and v_0; however, their impact on aw_0 is mainly canceled out due to the opposite signs of c_{u_0} and c_{v_0}.

After averaging u_0 and u_0^{I} to obtain an estimate of the self-consistent tadpole improvement factor $\bar{u}_0$, we observe that the volume dependence is at the level of 0.001% based on the spatial sizes utilized. On the other hand, the quark mass dependence appears to be more pronounced.

In the upper panel of Fig. 9, the value of $\bar{u}_0$ exhibits a linear behavior with respect to the combined quark mass $2\tilde{m}_l^{\text{PC}} + 0.55(1)\tilde{m}_s^{\text{PC}} \propto 0.5\tilde{m}_\pi^2 + 0.14\tilde{m}_{\eta_s}^2$. This suggests that the dependence on the strange quark mass exhibits a similar suppression as observed in a_{w_0}, as shown in

TABLE V. The tadpole improvement factors u_0^{I} and v_0^{I} used in the gauge and fermion actions, u_0 and v_0 measured from the realistic configurations generated using u_0^{I} and v_0^{I}, and their averages $\bar{u}_0$ and $\bar{v}_0$.

	C24P34	C24P29	C32P29	C32P23	C48P23	C48P14	F32P30	F48P30	F32P21	F48P21	H48P32
u_0^{I}	0.855453	0.855453	0.855453	0.855520	0.855520	0.855548	0.863437	0.863473	0.863488	0.863499	0.873378
u_0	0.855255(7)	0.855439(2)	0.855429(2)	0.855528(2)	0.855523(1)	0.855530(2)	0.863460(1)	0.863459(1)	0.863519(2)	0.863515(1)	0.873372(1)
$\bar{u}_0$	0.855354(4)	0.855446(1)	0.855441(1)	0.855524(1)	0.855522(1)	0.855539(1)	0.863449(1)	0.863466(1)	0.863504(1)	0.863507(1)	0.873375(1)
v_0^{I}	0.951479	0.951479	0.951479	0.951545	0.951545	0.951570	0.956942	0.956984	0.957017	0.957006	0.963137
v_0	0.951275(6)	0.951461(2)	0.951452(2)	0.951550(2)	0.951547(1)	0.951554(2)	0.956968(1)	0.956967(1)	0.957024(1)	0.957019(1)	0.963134(1)
$\bar{v}_0$	0.951377(3)	0.951470(1)	0.951466(1)	0.951548(1)	0.951546(1)	0.951562(1)	0.956955(1)	0.956976(1)	0.957021(1)	0.957013(1)	0.963136(1)

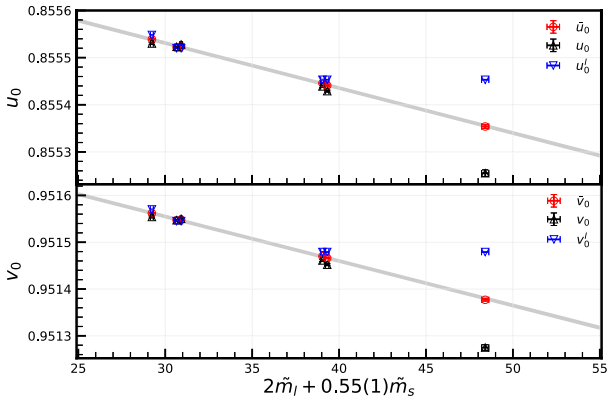

FIG. 9. The combined quark mass $2\tilde{m}_l^{\mathrm{PC}} + 0.55(1)\tilde{m}_s^{\mathrm{PC}}$ dependence of $\bar{u}_0 = \frac{u_0+u_0^l}{2}$ (upper panel) and $\bar{v}_0 = \frac{v_0+v_0^l}{2}$ (lower panel), at $10/g^2 = 6.2$.

Table IV. In the lower panel, we observe that v_0 exhibits the same quark mass dependence within the uncertainty.

However, such a mismatch will not significantly alter the physical observables. To illustrate this, let us consider the C24P34 ensemble with the largest mismatch effect. We calculate the pion two-point function $C_{2,wp}^{PP}(t;\tilde{m}_l^b, c_{\mathrm{sw}})$ using the same $\tilde{m}_l^b = -0.2770$, but with either $c_{\mathrm{sw}} = 1/(v_0^I)^3$ or $1/\bar{v}_0^3$. The joint-fit parameters defined in Eqs. (A5)–(A7) are listed in Table VI. We find that the matrix elements $\tilde{f}_{\mathrm{PS}}$ and Zwp remain unchanged within 0.05% uncertainties. However, $\tilde{m}_{\mathrm{PS}}$ experiences a 0.6% change, resulting in a 1.1% shift in the quark mass. This can be understood by noting that increasing c_{sw} leads to an increase in $\tilde{m}_{\mathrm{crti}}$, thereby making the multiplicative renormalizable quark mass $\tilde{m}_l^{\mathrm{PC}}$ larger for the same $\tilde{m}_l^b$. Consequently, the mismatch effect falls within the statistical uncertainty of C24P34 and is an order of magnitude smaller in other ensembles. Hence, we can safely disregard this mismatch effect in the subsequent discussions.

2. Renormalization

Unlike the hadron spectrum, the determination of hadron matrix elements on the lattice using discretized actions requires additional renormalization. The RCs defined under the $\overline{\mathrm{MS}}$ scheme, can only be obtained through regularization-independent (RI) schemes such as RI/MOM [29] or SMOM [30,31]. These RCs should be independent of intermediate schemes.

TABLE VI. The joint-fit results with the same $\tilde{m}_l^b$ and either $c_{\mathrm{sw}} = 1/(v_0^I)^3$ or $1/\bar{v}_0^3$, on the test ensemble C24P34 which has the largest mismatch effect.

	$\tilde{m}_{\mathrm{PS}}$	$\tilde{m}_l^{\mathrm{PC}}$	$\tilde{f}_{\mathrm{PS}}$	Z_{wp}
$1/(v_0^I)^3 = 1.1609$	0.1832(12)	0.01191(13)	0.0768(10)	10.50(30)
$1/(\bar{v}_0)^3 = 1.1613$	0.1822(12)	0.01178(13)	0.0768(11)	10.50(31)
Difference	0.0011(01)	0.00013(01)	0.0000(00)	0.00(01)

TABLE VII. Summary of uncertainties of RCs in percentage on the C32P29 ensemble through the intermediate RI/MOM scheme.

Source	$Z_q^{\overline{\mathrm{MS}}}/Z_V$ (%)	$Z_S^{\overline{\mathrm{MS}}}/Z_V$ (%)	$Z_P^{\overline{\mathrm{MS}}}/Z_V$ (%)	$Z_T^{\overline{\mathrm{MS}}}/Z_V$ (%)
Statistical error	0.13	0.37	0.92	0.06
Lattice spacing	< 0.01	< 0.01%	< 0.01	< 0.01
Finite volume effect	0.03	0.24	0.62	0.02
Fit range of $a^2\mu^2$	0.11	0.47	1.21	0.31
$\Lambda_{\mathrm{QCD}}^{\overline{\mathrm{MS}}}$	< 0.01	1.64	1.65	< 0.01
Truncation in matching	0.24	3.45	3.45	0.24
Perturbative running	0.02	0.07	0.07	0.02
Total	0.32	3.74	4.26	0.31

For the overlap fermion action, which possesses explicit chiral symmetry, the relations $Z_V = Z_A$ and $Z_P = Z_S = 1/Z_m$ are guaranteed. The consistency of using RI/MOM or SMOM schemes has been verified within systematic uncertainties [38]. However, in the case of the clover fermion action, which exhibits additive chiral symmetry breaking, additional considerations and discussions regarding its impact on renormalization are necessary in this section.

Following a similar strategy employed by Ref. [38], the values of $Z_{S,P,T}$ incorporate two sources of uncertainty. The first one encompasses ensemble-independent statistical and systematic uncertainties, including lattice spacing, finite volume effects, and $a^2\mu^2$ fit range. The second source of uncertainty arises from perturbative matching, including uncertainties associated with Λ_{QCD}, truncation in the perturbative matching, and perturbative scale running. These uncertainties are fully correlated across different ensembles. As shown in Table VII for the C32P29 ensemble, the truncation error is the largest source of uncertainty for $Z_{S,P}$.

In Ref. [38], the truncation error resulting from the 3-loop perturbative matching between the RI/MOM and $\overline{\mathrm{MS}}$ schemes is estimated by introducing a fake 4-loop correction. As an illustration, considering the scalar/pseudoscalar case with the largest truncation error, the 3-loop matching and the fake 4-loop one are expressed as follows:

$$C_{S,n_f=3,3-\mathrm{loop}}^{\overline{\mathrm{MS}},\mathrm{RI/MOM}} = 1 + 0.4244\alpha_s + 1.007\alpha_s^2 + 2.722\alpha_s^3, \quad \text{(A13)}$$

$$C_{S,n_f=3,\mathrm{fake4-loop}}^{\overline{\mathrm{MS}},\mathrm{RI/MOM}} = 1 + 0.4244\alpha_s + 1.007\alpha_s^2 + 2.722\alpha_s^3 + 7.358\alpha_s^4. \quad \text{(A14)}$$

The coefficient of fake α_s^4 term $2.722^2/1.007 = 7.358$ is the same as that provided by the Padé approximation,

$$C^{\overline{\mathrm{MS}},\mathrm{RI/MOM}}_{S,n_f=3,\mathrm{Pade}_3} = \frac{1-2.279\alpha_s-0.1402\alpha_s^2}{1-2.703\alpha_s} = 1+0.4244\alpha_s+1.007\alpha_s^2+2.722\alpha_s^3 + 7.358\alpha_s^4+\mathcal{O}(\alpha_s^5). \quad \text{(A15)}$$

Based on the precise 4-loop calculation, the precise 4-loop matching is [49],

$$C^{\overline{\mathrm{MS}},\mathrm{RI/MOM}}_{S,n_f=3,4-\mathrm{loop}} = 1+0.4244\alpha_s+1.007\alpha_s^2+2.722\alpha_s^3 + 8.263\alpha_s^4, \quad \text{(A16)}$$

which is larger than $C^{\overline{\mathrm{MS}},\mathrm{RI/MOM}}_{S,n_f=3,\mathrm{fake}\,4-\mathrm{loop}}$ but smaller than $C^{\overline{\mathrm{MS}},\mathrm{RI/MOM}}_{S,n_f=3,\mathrm{Pade}_3}$. Considering that the existence of the 5-loop correction, we anticipate that the Padé approximation will provide a more accurate estimate for $C_{S,n_f=3}$.

Thus, we shall use the 4-loop Padé approximation,

$$C^{\overline{\mathrm{MS}},\mathrm{RI/MOM}}_{S,n_f=3,\mathrm{Pade}_4} = \frac{1-2.611\alpha_s-0.2813\alpha_s^2-0.3349\alpha_s^3}{1-3.036\alpha_s} = 1+0.4244\alpha_s+1.007\alpha_s^2+2.722\alpha_s^3 + 8.263\alpha_s^4+25.084\alpha_s^5+\mathcal{O}(\alpha_s^6), \quad \text{(A17)}$$

as the central value of the matching coefficient, and taking the difference between $C_{S,n_f=3,\mathrm{Pade}_4}$ and $C_{S,n_f=3,\mathrm{Pade}_3}$ as systematic uncertainty of the truncation on the perturbative matching.

In this section, we will commence with the vector current normalization and explore different choices of quark field renormalization in Appendix A 2 a. Appendix A 2 a will then present the investigation of the chiral symmetry breaking effect between Z_V and Z_A. Subsequently, in Appendix A 2 d, we will examine the analogous investigation of Z_P and Z_S, with additional discussions on Z_m in Appendix A 2 c. Finally, for completeness, the case of the tensor current will be discussed in Appendix A 2 e.

a. Vector normalization and Z_q

Unlike its continuum counterpart, the local vector current under lattice regularization is subject to both the $\mathcal{O}(a^2)$ discretization error and $\mathcal{O}(\alpha_s)$-loop corrections [50], and then requires additional normalization. The normalization constant Z_V can be determined from the vector current conservation condition,

$$Z_V\frac{\langle H|V_4|H\rangle}{\langle H|H\rangle}=1, \quad \text{(A18)}$$

where $V_\nu=\bar\psi\gamma_\nu\psi$ and H represents an arbitrary hadronic state. Thus, extracting Z_V from the pion correlator in the rest frame will be the cheapest choice [50],

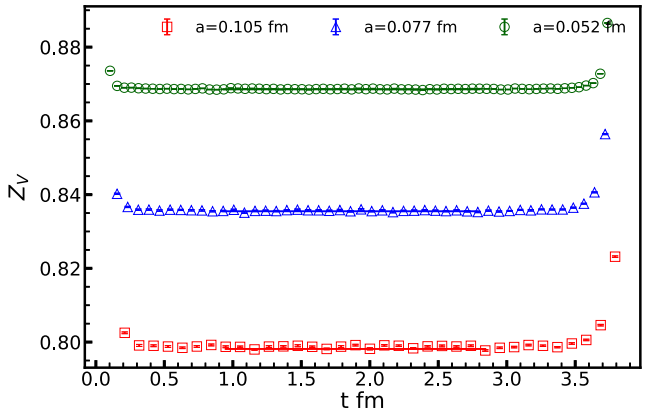

FIG. 10. Z_V from the vector current conservation of pion correlator at three lattice spacing. The plateau values are summarized in Table IX as the Z_V of the ensembles C24P29, F32P30, and H48P32.

$$Z_V=\sum_{\vec{x}}\langle \mathrm{Tr}[S_C^\dagger(\vec{x},\tilde{T}/2;0;m_q)S_C(\vec{x},\tilde{T}/2;0;m_q)]\rangle/ \times\left\{2\sum_{\vec{x},\vec{z}}\langle \mathrm{Tr}[S_C^\dagger(\vec{x},\tilde{T}/2;0;m_q)S(\vec{x},\tilde{T}/2;\vec{z},t;m_q) \times\gamma_t S_C(\vec{z},t;y_0;m_q)]\rangle\right\}|_{\tilde{T}\gg t\gg 0}, \quad \text{(A19)}$$

where the additional propagator in the denominator can be obtained using the sequential source technique. The ratio at three lattice spacing and their constant fits in the range of $0\ll t\ll\tilde{T}/2$, are shown in Fig. 10. As demonstrated in [50], Z_V is affected by α_s corrections and cannot be accurately extrapolated to 1 using a simple naive a^{2n} continuum extrapolation.

The quark field RC $Z_q^{\mathrm{RI}'}$ in the RI scheme can be accessed through either its definition,

$$Z_q^{\mathrm{RI}'}(\mu)=\lim_{m\to 0}\frac{-i}{12p^2}\mathrm{Tr}[S^{-1}(p)\not{p}]_{p^2=\mu^2}, \quad \text{(A20)}$$

with $S(p)=\sum_x e^{-ip\cdot x}\langle\psi(x)\bar\psi(0)\rangle$, or the vertex correction of the vector current which is equivalent in the continuum,

$$Z_q^{\mathrm{RI}',\mathrm{ver}}(\mu)=\lim_{m\to 0}\frac{Z_V}{36}\mathrm{Tr}\left[\Lambda_V^\mu(p,p)\left(\gamma_\mu-\frac{\not{p}p_\mu}{p^2}\right)\right]_{p^2=\mu^2}, \quad \text{(A21)}$$

where

$$\Lambda_{\mathcal{O}}(p_1,p_2)=S^{-1}(p_1)G_{\mathcal{O}}(p_1,p_2)S^{-1}(p_2), \quad G_{\mathcal{O}}(p_1,p_2)=\sum_{x,y}e^{-i(p_1\cdot x-p_2\cdot y)}\langle\psi(x)\mathcal{O}(0)\bar\psi(y)\rangle. \quad \text{(A22)}$$

These two definitions are equivalent in the continuum, but they are subject to different discretization errors. Figure 11

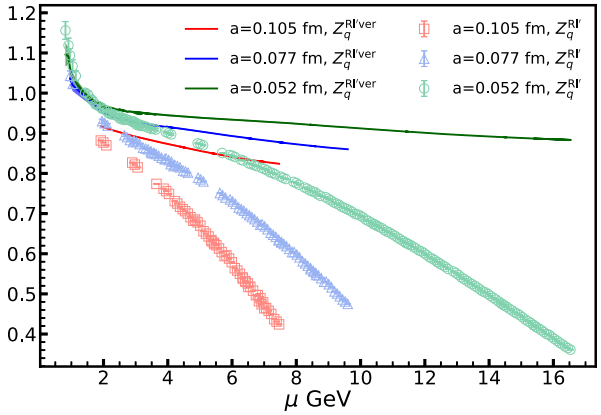

FIG. 11. Comparison of $Z_q^{\mathrm{RI}'}$ (data points) and $Z_q^{\mathrm{RI}',\mathrm{ver}}$ (bands) at three lattice spacing with different scale μ. The discrepancy observed in the figure is primarily attributed to the discretization error.

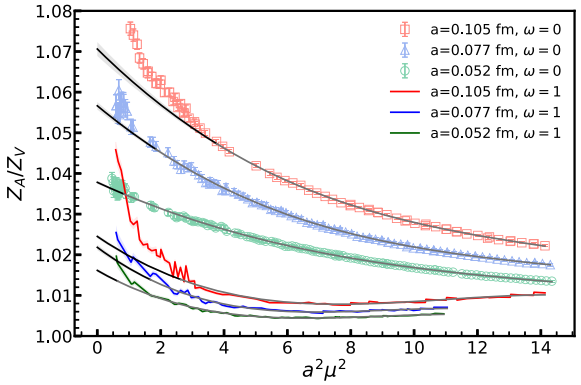

FIG. 12. The ratio Z_A/Z_V through the RI/MOM scheme (data points) or SMOM scheme (bands) at three lattice spacing as functions of a^2p^2.

illustrates the comparison between $Z_q^{\mathrm{RI}'}$ and $Z_q^{\mathrm{RI}',\mathrm{ver}}$ at three lattice spacings. The two definitions become closer either at smaller μ or smaller a, with $Z_q^{\mathrm{RI}',\mathrm{ver}}$ exhibiting a significantly smaller a^2p^2 error. This situation is reminiscent of the overlap fermions case [38], where the $a^2\mu^2$ errors have opposite signs.

Given that $Z_q^{\mathrm{RI}',\mathrm{ver}}$ involves an off-diagonal projection that introduces additional discretization errors, it is more convenient to define the quark field renormalization through the standard RI definition [29],

$$Z_q^{\omega}(\mu^2) = \lim_{m\to 0} \frac{Z_V}{48} \mathrm{Tr}[\Lambda_V^{\mu}(p_1,p_2)\gamma_\mu]_{p_1^2=p_2^2=\mu^2,(p_1-p_2)^2=\omega\mu^2}, \tag{A23}$$

The discrepancy between Z_q^{ω} with different ω and $Z_q^{\mathrm{RI}'}$ should be eliminated through their respective perturbative matchings, which can be calculated in the continuum. For the SMOM condition with $\omega = 1$, the convergence of the perturbative matching is poorer compared to that of Z_q using the q-projection definition [31], but the discretization error will be smaller.

b. Chiral symmetry breaking between Z_A and Z_V

For the clover fermion, the ratio

$$\frac{Z_A}{Z_V}(\mu^2,\omega) = \left.\frac{\mathrm{Tr}[\Lambda_A^{\mu,\overline{\mathrm{MS}}}(p_1,p_2)\gamma_5\gamma_\mu]}{\mathrm{Tr}[\Lambda_V^{\mu,\overline{\mathrm{MS}}}(p_1,p_2)\gamma_\mu]}\right|_{p_1^2=p_2^2=\mu^2,(p_1-p_2)^2=\omega\mu^2} \tag{A24}$$

can deviate from unity due to the additive chiral symmetry breaking present in the action. As depicted in Fig. 12 for the RI/MOM scheme (data points, $\omega = 0$) and SMOM scheme (bands, $\omega = 1$) at three different lattice spacings with $m_\pi \sim 300$ MeV, we observe that the breaking diminishes as $a^2\mu^2$ increases, indicating that the chiral symmetry breaking in the mass term becomes less important. However, the ratio does not approach unity in the continuum limit without any α_s corrections. It is worth noting that the breaking using the SMOM scheme is much smaller than that with the RI/MOM scheme, while increases rapidly at small $a^2\mu^2$.

If we fit the Z_A/Z_V data with a polynomial form in the range of $9\ \mathrm{GeV}^2 \le p^2 \le 15/a^2$ and extrapolate it to $a^2p^2 = 0$, the obtained result will be sensitive to the choice of ω. Therefore, we extrapolate the f_π at two coarser lattice spacings to the unitary pion mass at the finest lattice spacing, which is $m_\pi = 317$ MeV. The renormalized $f_\pi^R = Z_A f_\pi$ is shown in Fig. 13, using both the extrapolated Z_A/Z_V obtained through RI/MOM and SMOM. The results suggest that the scheme sensitivity is approximately 1% after a linear a^2 continuum extrapolation, with the discretization error through RI/MOM being 25% smaller.

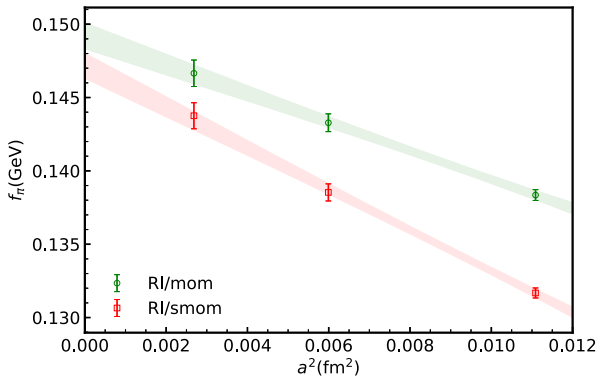

FIG. 13. Renormalized pion-decay constant f_π with $m_\pi = 317$ MeV at three lattice spacing, using $Z_A = Z_V\frac{Z_A}{Z_V}$ through either RI/MOM or SMOM scheme. The extrapolated values deviate by 1.3(8)%.

c. Pesudoscalar current renormalization Z_P and induced quark mass

The renormalization of m_q^{PC} requires both Z_A and Z_P. By defining $\hat{Z}_P^\omega$ under either the RI/MOM ($\omega = 0$) or SMOM ($\omega = 1$) scheme,

$$\hat{Z}_P^\omega(\mu) = \frac{Z_q^\omega}{\frac{1}{12}\mathrm{Tr}[\Lambda_P(p_1,p_2)\gamma_5]}\Big|_{p_1^2=p_2^2=\mu^2,(p_1-p_2)^2=\omega\mu^2} = Z_V \frac{\frac{1}{48}\mathrm{Tr}[\Lambda_V^\mu(p_1,p_2)\gamma_\mu]}{\frac{1}{12}\mathrm{Tr}[\Lambda_P(p_1,p_2)\gamma_5]}\Big|_{p_1^2=p_2^2=\mu^2,(p_1-p_2)^2=\omega\mu^2}, \tag{A25}$$

Z_P in the chiral limit can be extracted from the following parametrization:

$$\hat{Z}_P^\omega(\mu; m_q^{\mathrm{PC}}) = \left[\frac{A_P^\omega(\mu)}{m_q^{\mathrm{PC}}} + (Z_P^\omega(\mu))^{-1} + C_P^\omega(\mu) m_q^{\mathrm{PC}}\right]^{-1}, \tag{A26}$$

where m_q^{PC} can be replaced by m_π^2 based on the GMOR relation. As shown in Fig. 14, $A_P^{\omega=1}$ is negligible in the fit, but $A_P^{\omega=0}$ will be nonzero due to the mass pole of the Goldstone meson and is related to the dynamical quark mass under the Landau gauge [51].

If one define the RI quark mass at given scale as [51]

$$m_q^{\mathrm{RI}} = \frac{\frac{1}{12}\mathrm{Tr}[S^{-1}(p)]|_{p^2=\mu^2}}{Z_q^{\mathrm{RI}}(\mu)}, \tag{A27}$$

then for the overlap fermion action with exact chiral symmetry, we can further define $Z_m^{\mathrm{RI}} = m_q^{\mathrm{RI}}/m_q^b$ and have the relation $Z_m \hat{Z}_p = 1$ holding for arbitrary m_q and μ. Thus, the following definition of the RI quark mass:

$$\hat{m}_q^{\mathrm{RI}} = \frac{Z_A m_q^{\mathrm{PC}}}{\hat{Z}_P^{\mathrm{MOM}}(\mu)}, \tag{A28}$$

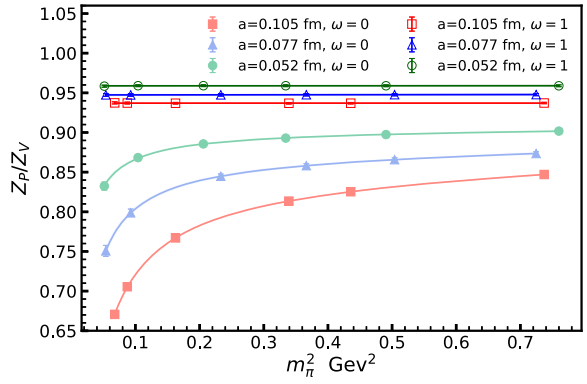

FIG. 14. Valence pion mass square $m_{\pi,vv}^2$ dependence of $\hat{Z}_P^{\omega=0}$ (RI/MOM, lighter points) and $\hat{Z}_P^{\omega=1}$ (SMOM, darker points) with $a^2\mu^2 = 4$, at three lattice spacing and $m_{\pi,ss} \sim 300$ MeV.

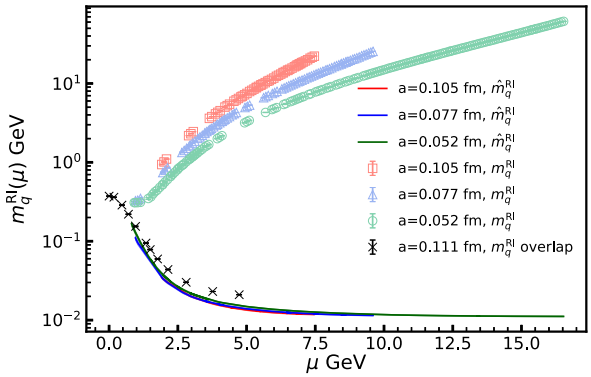

FIG. 15. Values of m_q^{RI} (data points) and $\hat{m}_q^{\mathrm{RI}}$ (bands) at three lattice spacing with $m_\pi \sim 300$ MeV at different RI/MOM scale μ. $\hat{m}_q^{\mathrm{RI}}$ (black crosses) using the overlap fermion are also shown on the figure for comparison.

ensures that $m_q^{\mathrm{RI}} = \hat{m}_q^{\mathrm{RI}}$ given the relation $Z_A m_q^{\mathrm{PC}} = m_q^b$ for the overlap fermion. However, the case of clover fermions can be quite different due to its additive chiral symmetry breaking.

In Fig. 15, we present both m_q^{RI} and $\hat{m}_q^{\mathrm{RI}}$ at three lattice spacings with $m_\pi \sim 300$ MeV, and compare them with the results obtained from the overlap fermion at $a = 0.111$ fm. We observe that $\hat{m}_q^{\mathrm{RI}}$ seems to be insensitive to the lattice

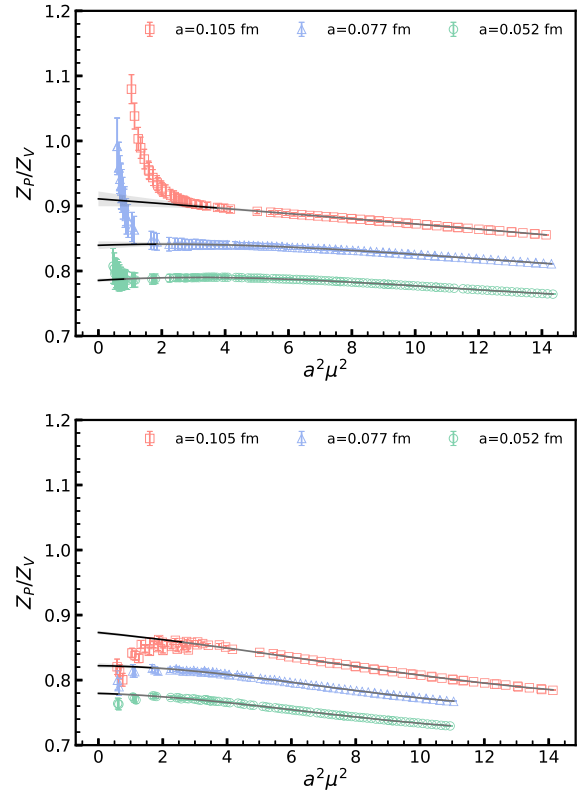

FIG. 16. $a^2\mu^2$ dependence of $Z_P^{\overline{\mathrm{MS}}(2\ \mathrm{GeV})}$ through the RI/MOM ($\omega = 0$, upper panel) and SMOM ($\omega = 1$, lower panel) schemes, at three lattice spacing and $m_{\pi,ss} \sim 300$ MeV.

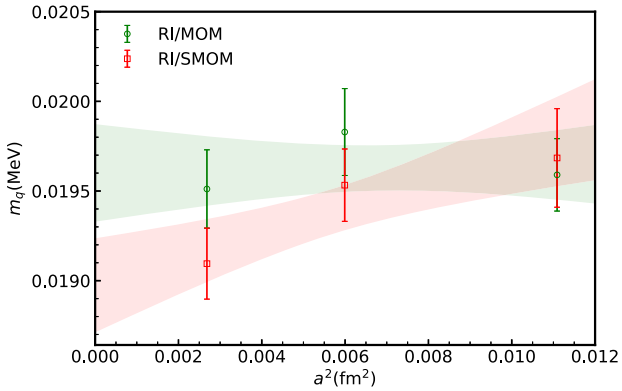

FIG. 17. Renormalized quark mass with $m_\pi = 317$ MeV at three lattice spacing, using $Z_P^{\overline{\rm MS}(2\ {\rm GeV})}$ through either RI/MOM or SMOM scheme. The extrapolated values deviate by 3.1(1.5)%.

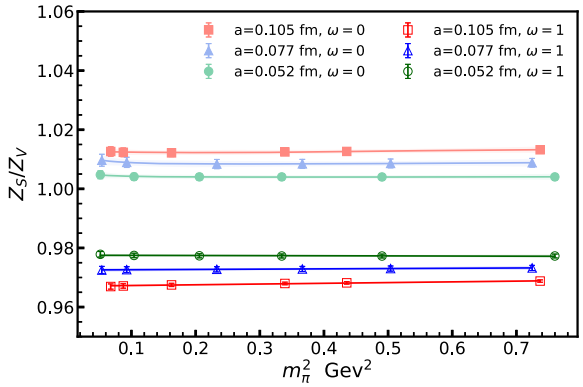

FIG. 18. Valence pion mass square $m^2_{\pi,vv}$ dependence of $\hat{Z}_S^{\omega=0}$ (RI/MOM, lighter points) and $\hat{Z}_P^{\omega=1}$ (SMOM, darker points) with $a^2\mu^2 = 4$, at three lattice spacing and $m_{\pi,ss} \sim 300$ MeV.

spacing and is close to the overlap result $\hat{m}_q^{\rm RI} = m_q^{\rm RI}$ [51]; but $m_q^{\rm RI}$ exhibits a significant $a^2\mu^2$ error and some unknown UV effects, resulting in large values at large μ.

After Z_P^ω is extracted, it can be further converted to the $\overline{\rm MS}$ scheme at given scale likes $\mu_0 = 2$ GeV through the perturbative matching, and shall be independent of both μ and ω. In Fig. 16, $Z_P^{\overline{\rm MS}(2\ {\rm GeV})}$ obtained through the RI/MOM scheme at the coarsest lattice spacing $a = 0.105$ fm can be consistent with that using the SMOM scheme, with the 3–4% systematic uncertainties from the perturabative matching. The situation improves at smaller lattice spacing, and systematic uncertainties are also smaller there. In Fig. 17, we show the renormalized quark mass at $\overline{\rm MS}(2\ {\rm GeV})$ with $m_\pi = 317$ MeV at three lattice spacing, using $Z_P^{\overline{\rm MS}(2\ {\rm GeV})}$ through either RI/MOM or SMOM scheme. We can see that the lattice spacing dependence using the RI/MOM scheme is consistent with zero, while SMOM shows a nonvanishing dependence and make the continuum extrapolated value to be 3.1 (1.5)% lower.

d. Chiral symmetry breaking between Z_P and Z_S

The scalar current RC can be defined similarly with a slightly different parametrization,

$$\hat{Z}_S^\omega(\mu) = Z_V \frac{\frac{1}{48}{\rm Tr}[\Lambda_V^\mu(p_1,p_2)\gamma_\mu]}{\frac{1}{12}{\rm Tr}[\Lambda_S(p_1,p_2)]}\bigg|_{p_1^2=p_2^2=\mu^2,(p_1-p_2)^2=\omega\mu^2},$$
$$\hat{Z}_S^\omega(\mu; m_q^{\rm PC}) = \frac{A_S^\omega(\mu)}{m_q^{\rm PC}} + (Z_S^\omega(\mu)) + C_S^\omega(\mu) m_q^{\rm PC}, \qquad \text{(A29)}$$

where $S = \bar{\psi}\psi$, and the A_S^ω term can be dropped for $\omega = 1$. However, as shown in Fig. 18, the effect of the A_S^ω term is consistently negligible regardless of the value of ω.

After converting to the $\overline{\rm MS}$ scheme at a given scale using the same matching procedure as in the pseudoscalar case, we obtain $Z_S^{\overline{\rm MS}(2\ {\rm GeV})}$ as shown in Fig. 19, through either the RI/MOM scheme (upper panel) or the SMOM scheme (lower panel) with the corresponding $a^2\mu^2$ errors. We observe that the scheme dependence of Z_S is much stronger than that of Z_P, but the difference diminishes as the lattice spacing decreases.

Another comparison we can make is the ratio Z_S/Z_P obtained through either the RI/MOM or SMOM scheme.

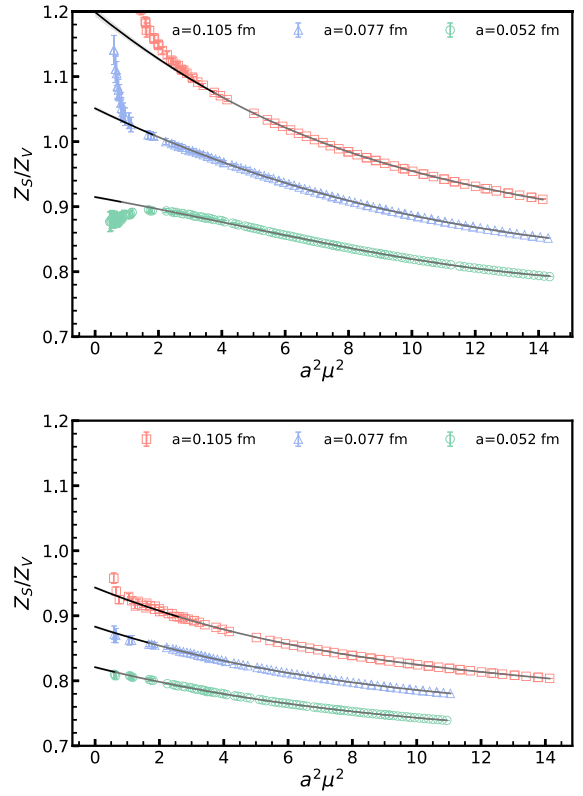

FIG. 19. $a^2\mu^2$ dependence of $Z_S^{\overline{\rm MS}(2\ {\rm GeV})}$ through the RI/MOM ($\omega = 0$, upper panel) and SMOM ($\omega = 1$, lower panel) schemes, at three lattice spacing and $m_{\pi,ss} \sim 300$ MeV.

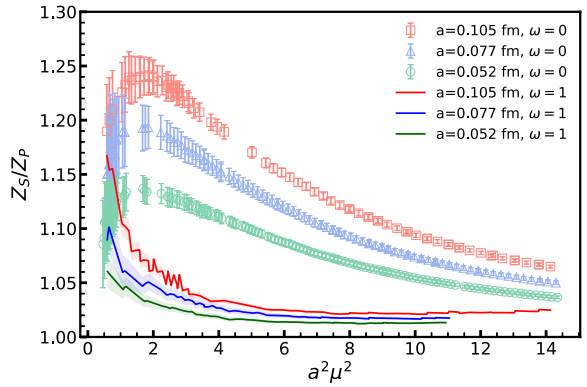

FIG. 20. The ratio Z_S/Z_P through the RI/MOM scheme at three lattice spacing as functions of a^2p^2.

As depicted in Fig. 20, the chiral symmetry breaking effect is significantly smaller when using the SMOM scheme (bands) compared to the RI/MOM scheme (data points). Moreover, both schemes exhibit further suppression at smaller lattice spacings. Similar to the Z_A/Z_V case, the inclusion of the $\mathcal{O}(\alpha_s)$ term is necessary to restore chiral symmetry in the continuum.

e. Z_T and brief summary on renormalization

For completeness, we also show the tensor current renormalization using both the RI/MOM and SMOM schemes,

$$\hat{Z}_T^{\omega}(\mu) = Z_V \frac{\frac{1}{48}\mathrm{Tr}[\Lambda_V^{\mu}(p_1,p_2)\gamma_\mu]}{\frac{1}{72}\mathrm{Tr}[\Lambda_{T_{\mu\nu}}(p_1,p_2)\sigma_{\mu\nu}]}\Big|_{p_1^2=p_2^2=\mu^2,(p_1-p_2)^2=\omega\mu^2}, \tag{A30}$$

where $T_{\mu\nu} = \bar{\psi}\sigma_{\mu\nu}\psi$. Then $Z_T^{\overline{\mathrm{MS}}(2\ \mathrm{GeV})}$ can be obtained through the corresponding perturbative matching after performing a linear m_π^2 extrapolation to the continuum, as shown in Fig. 21. The systematic uncertainty arising from the SMOM matching is estimated to be 2–3%, which implies that $Z_T^{\overline{\mathrm{MS}}(2\ \mathrm{GeV})}$ is considered independent of the intermediate scheme within this uncertainty. At last, $a^2\mu^2$ dependence of $Z_T^{\overline{\mathrm{MS}}(2\ \mathrm{GeV})}$ is showed in Fig. 22.

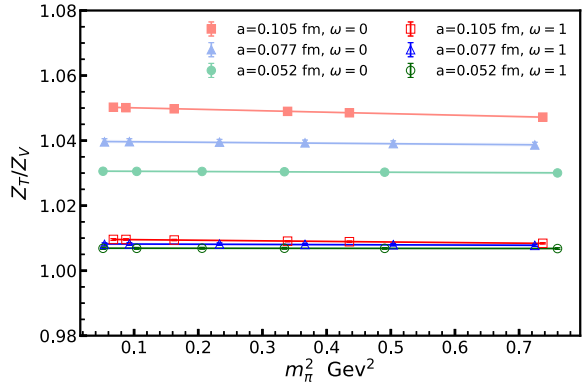

FIG. 21. Valence pion mass square $m_{\pi,vv}^2$ dependence of $\hat{Z}_S^{\omega=0}$ (RI/MOM, lighter points) and $\hat{Z}_T^{\omega=1}$ (SMOM, darker points) with $a^2\mu^2 = 4$, at three lattice spacings and $m_{\pi,ss} \sim 300$ MeV.

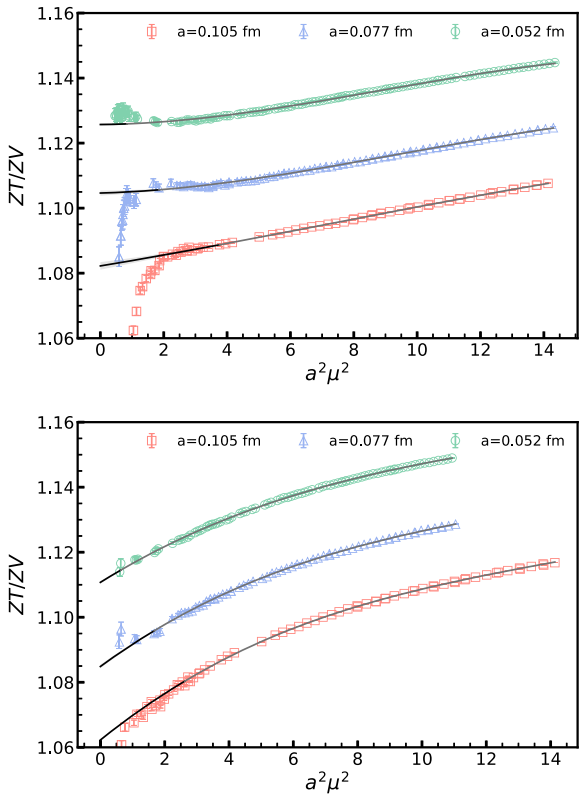

FIG. 22. $a^2\mu^2$ dependence of $Z_T^{\overline{\mathrm{MS}}(2\ \mathrm{GeV})}$ through the RI/MOM ($\omega = 0$, upper panel) and SMOM ($\omega = 1$, lower panel) schemes, at three lattice spacing and $m_{\pi,ss} \sim 300$ MeV.

Based on the values of $Z_{A,S,P,T}$ obtained in this work and collected in Table VIII, it can be observed that the dependence on the intermediate scheme (RI/MOM or

TABLE VIII. Normalization and renormalization constant at $\overline{\mathrm{MS}}(2\ \mathrm{GeV})$ at three lattice spacing with $m_{\pi,ss} \sim 300$ MeV, using RI/MOM ($\omega = 0$) or SMOM ($\omega = 1$) as intermediate scheme.) In the RI/MOM case, the first line represents the result fit without $1/p^2$ term, while the second line represents the fit with that term.

a (fm)	ω	Z_A	Z_S	Z_P	Z_T
0.1053(2)	0	0.8547(13)	0.957(08)(34)	0.727(09)(26)	0.864(01)(05)
		0.8388(39)	0.897(20)(44)	0.672(36)(31)	0.867(04)(04)
	1	0.8177(04)	0.754(02)(09)	0.698(05)(08)	0.848(01)(27)
0.0775(2)	0	0.8821(08)	0.879(05)(18)	0.701(05)(15)	0.923(01)(03)
		0.8792(25)	0.892(12)(11)	0.689(22)(09)	0.919(05)(02)
	1	0.8533(06)	0.738(01)(07)	0.689(02)(06)	0.906(01)(22)
0.0519(3)	0	0.9011(04)	0.796(09)(10)	0.683(05)(08)	0.978(01)(02)
		0.8998(07)	0.822(08)(04)	0.683(08)(03)	0.973(01)(01)
	1	0.8838(02)	0.720(01)(05)	0.684(01)(05)	0.961(00)(19)

TABLE IX. Normalization and renormalization constants at $\overline{\text{MS}}(2\ \text{GeV})$ on all the ensembles. The RCs include two uncertainties where the former one is the ensemble independent statistical and systematic uncertainties, and the latter one is the systematic uncertainties from the perturbative matching which are fully correlated on different ensembles.

	C24P34	C24P29	C32P29	C32P23	C48P23	C48P14	F32P30	F48P30	F32P21	F48P21	H48P32
Z_V	0.79676(32)	0.79814(23)	0.79810(13)	0.79957(13)	0.79954(05)	0.79957(06)	0.83548(12)	0.83511(04)	0.83579(09)	0.83567(05)	0.86855(04)
Z_A	0.85698(89)	0.85442(85)	0.8547(13)	0.85593(87)	0.85674(96)	0.85605(94)	0.88161(64)	0.88213(77)	0.88069(60)	0.88063(98)	0.90113(36)
Z_S	0.960(05)(33)	0.953(06)(31)	0.957(08)(34)	0.957(06)(33)	0.966(10)(34)	0.963(04)(34)	0.871(09)(22)	0.879(05)(18)	0.871(06)(21)	0.878(04)(17)	0.796(09)(10)
Z_P	0.732(11)(26)	0.733(13)(24)	0.727(09)(26)	0.733(08)(26)	0.733(09)(27)	0.727(11)(26)	0.699(07)(17)	0.701(05)(15)	0.704(05)(17)	0.701(08)(15)	0.683(05)(08)
Z_T	0.865(02)(05)	0.864(01)(05)	0.864(01)(05)	0.865(01)(05)	0.865(01)(05)	0.866(01)(05)	0.922(01)(04)	0.923(01)(03)	0.920(01)(04)	0.922(01)(03)	0.978(01)(02)

SMOM) is reduced as the lattice spacing decreases. However, it is important to note that the scheme dependence is not completely eliminated even after performing the continuum extrapolation. Considering the lattice spacing dependence of the renormalized f_π, m_q, and g_S, it is recommended to use the RI/MOM scheme to suppress the discretization error.

In Table VIII, we also show the renormalization constants using the RI/MOM scheme but with an additional $1/p^2$ term [32]. This term can have an obvious impact at the coarsest lattice spacing but is consistent with zero at the finest lattice spacing. This is understandable as the fitting range at finer lattice spacing is much larger, reducing the possible influence of a $1/p^2$ pole in the inferred region. Thus, it can be considered a discretization effect that will be eliminated in the continuum extrapolation.

As a summary of this section, Table IX summarizes the normalization and renormalization constants for all the ensembles used in this work, obtained through the intermediate RI/MOM scheme. The first uncertainty of RCs is ensemble independent, while the second one is fully correlated on different ensembles and can be suppressed after the continuum extrapolation.

3. Global fit

In order to process this continuum extrapolation systematically, we calculate the quark propagators with unitary light quark mass and also two partially quenched quark masses with the constraint $m_\pi L > 3.5$, on each of the 11 ensembles. Then we use the following NLO partially quenched χPT form [41] to describe the pion masses and decay constants with different valence and sea quark masses, in addition to extra parameters $c_{m/f,a/l}$ for the finite lattice spacing/volume corrections:

$$\begin{aligned} m^2_{\pi,\mathrm{vv}} = \Lambda_\chi^2 2y_\mathrm{v}\Big\{1 + \frac{2}{N_f}[(2y_\mathrm{v} - y_\mathrm{s})\ln(2y_\mathrm{v}) + (y_\mathrm{v} - y_\mathrm{s})] \\ + 2y_\mathrm{v}(2\alpha_8 - \alpha_5) + 2y_\mathrm{s}N_f(2\alpha_6 - \alpha_4)\Big\} \\ \times [1 + c_L^\pi e^{-m_\pi L} + c_s^\pi(m^2_{\eta_s} - m^2_{\eta_s,\mathrm{phys}})] \\ \times (1 + c_a^\pi a^2), \end{aligned} \tag{A31}$$

$$\begin{aligned} F_{\pi,\mathrm{vv}} = F\left(1 - \frac{N_f}{2}(y_\mathrm{v} + y_\mathrm{s})\ln(y_\mathrm{v} + y_\mathrm{s}) + y_\mathrm{v}\alpha_5 + y_\mathrm{s}N_f\alpha_4\right) \\ \times [1 + d_L^\pi e^{-m_\pi L} + d_s^\pi(m^2_{\eta_s} - m^2_{\eta_s,\mathrm{phys}})] \\ \times (1 + d_a^\pi a^2), \end{aligned} \tag{A32}$$

where $N_f = 2$ for two light flavors and $\Lambda_\chi = 4\pi F$ is the intrinsic scale of χPT with F being the pion decay constant in the chiral limit. The dimensionless expansion parameters $y_{\mathrm{v/s}} = \frac{\Sigma m_l^{\mathrm{v/s}}}{F^2\Lambda_\chi^2}$ involve the chiral condensate Σ and quark mass

$m_{v/s}$ for the valence and sea quark masses, respectively. Additionally, α_i represents the NLO low-energy constants of χPT at the intrinsic scale Λ_χ. These constants can be converted to the usual scale-dependent partially quenched χPT NLO coefficients as $L_i(\mu) = \frac{1}{128\pi^2}(\alpha_i + c_i \ln\frac{\mu}{\Lambda_\chi})$ with $c_{4,5,6,8} = \{-\frac{1}{2}, -\frac{N_f}{2}, -\frac{2+N_f^2}{N_f^2}, \frac{N_f^2-4}{4N_f}\}$, respectively [52,53]. We also introduce additional corrections terms with the coefficients $c_{m/f,a/L/s}$ to account for the discretization, finite volume and strange quark mismatch effects, with $m_{\eta_s} = 689.63(18)$ MeV from Ref. [48].

Since the statistics on each ensemble are different, we perform 4000 bootstrap resamplings on each ensemble and conduct the correlated global fit based on these bootstrap samples. In such a strategy, the correlation between different ensembles vanishes within the statistical uncertainty of the resampling and is suppressed by the number of bootstrap samples. The lattice spacing and renormalization constants are sampled for each bootstrap sample using a Gaussian distribution with their uncertainties as the width of the distribution. These values are then applied to the dimensionless quantities extracted from the joint fit defined in Eqs. (A5)–(A8).

The lattice spacing uncertainty is sampled with an uniform seed at a given lattice spacing, since this uncertainty is fully corrected on all the ensembles at this lattice spacing. Similarly, The perturbative matching uncertainty of Z_P is sampled with a uniform seed on all the ensembles, but with respective rescale factors on each ensemble. On the other hand, the uncertainty of lattice spacing and the nonperturbative uncertainty of Z_P are sampled independently on each ensemble. In order to show the impact of two Z_P uncertainties in the global fit, we preform the following four cases of fit, and show the results of Σ, F, $\alpha_{4,5,6,8}$, and also $c_{m/f,a/L/s}$ in Table X:

(1) Fitting with the statistical uncertainty $\delta\tilde{O}$ from the dimensionless observable $\tilde{O}$ with $O = m_\pi, m_q^{\mathrm{PC}}$, and f_π, and also lattice spacing uncertainty δa.
(2) Fitting with $\delta\tilde{O}$, δa and nonperturbative uncertainty $\delta_{\mathrm{np}} Z_P$.
(3) Fitting with $\delta\tilde{O}$, δa and perturbative uncertainty $\delta_{\mathrm{p}} Z_P$.
(4) Fitting with $\delta\tilde{O}$, δa, $\delta_{\mathrm{np}} Z_P$ and also $\delta_{\mathrm{p}} Z_P$.

All four cases provide reasonable χ^2/d.o.f. values, and similar values of F which are irrelevant to Z_P. However, the uncertainty of Σ is highly sensitive to δZ_P, as expected. By imposing the conditions $y_{\mathrm{s}} = y_{\mathrm{v}}$, $M_{\pi,\mathrm{vv}} = M_{\pi,\mathrm{phys}} = 134.98$ MeV, $a \to 0$, and $L \to \infty$, we can extract the light quark mass $m_l^{\overline{\mathrm{MS}}(2\ \mathrm{GeV})}$ in the continuum and infinite volume limits from the global fit. The m_l obtained from different cases of fits are also listed in Table X.

As shown in the table, the extrapolated quark mass $m_l = 3.60(3)$ MeV obtained in Case (1) is consistent with the value 3.64(8)(11) MeV at $a = 0.105$ fm, as we argued before. Additionally, it has a smaller uncertainty due to the constraints from the other ensembles and the exclusion of δZ_P. However, the uncertainty is enlarged to 2.7% in Case (4) where both the nonperturbative and perturbative uncertainties of Z_P are included, while the central value remains almost unchanged. Treating $\delta_{\mathrm{p}} Z_P$ as correlated across all the ensembles significantly suppresses its impact from 3% (at $a = 0.105$ fm) to 0.5% after the continuum extrapolation, as shown in Case (3); However, Case (2) suggests that the $\delta_{\mathrm{np}} Z_P$ is enlarged from 1% (at $a = 0.105$ fm) to 2.5% simultaneously since it is independent for different ensembles.

TABLE X. Global fits with and without nonperturabtive uncertainty $\delta_{\mathrm{np}} Z_P$ and perturabtive uncertainty $\delta_{\mathrm{p}} Z_P$.

δZ_P included	N/A	δ_{np}	δ_{p}	$\delta_{\mathrm{np}} + \delta_{\mathrm{p}}$
χ^2/d.o.f.		1.3		
F (GeV)	0.08659(69)	0.08659(72)	0.08659(71)	0.08660(74)
$\Sigma^{1/3}$ (GeV)	0.2684(14)	0.2685(30)	0.2685(14)	0.2686(36)
α_4	0.342(93)	0.343(99)	0.340(99)	0.34(10)
α_5	−0.38(18)	−0.39(19)	−0.38(18)	−0.38(20)
α_6	0.056(41)	0.058(84)	0.054(47)	0.054(86)
α_8	0.482(79)	0.48(18)	0.483(81)	0.48(18)
c_a^π (fm^{-2})	2.12(67)	2.1(1.8)	2.1(3.7)	2.0(4.1)
c_L^π	0.64(20)	0.65(53)	0.64(20)	0.65(51)
c_s^π (GeV^2)	0.058(32)	0.06(14)	0.101(32)	0.07(14)
d_a^π (fm^{-2})	−5.56(45)	−5.55(47)	−5.57(55)	−5.57(57)
d_L^π	−0.73(14)	−0.73(15)	−0.73(14)	−0.73(15)
d_s^π (GeV^2)	0.197(28)	0.197(31)	0.197(29)	0.198(32)
$m_{l,\mathrm{phys}}$ (MeV)	3.600(31)	3.60(11)	3.60(03)	3.60(11)
$f_{\pi,\mathrm{phys}}$ (MeV)	130.73(89)	130.73(90)	130.73(90)	130.74(92)

It is worth mentioning that the relative uncertainty of Σ and m_l in Cases (2)–(4) is almost the same and will be canceled when we consider the renormalization independent combination Σm_l.

Currently, 90% of the uncertainty of $m_l = 3.60(11)$ MeV comes from the independent statistical uncertainty of Z_P using the RI/MOM scheme on different ensembles, which can be suppressed if we adopt a more aggressive treatment on the renormalization constants. However, the current 3% uncertainty of m_l is similar to the difference between the continuum extrapolation of m_l at $m_\pi = 317$ MeV using either the RI/MOM or SMOM scheme. Therefore, we reserve this opinion for future study, where more lattice spacings can be utilized to gain a better understanding of the chiral symmetry breaking effect in the renormalization constants.

With the m_l extracted above, we can also determine the physical f_π in the continuum and infinite volume limits to be 130.7(9) MeV, which is consistent with the experimental value of 130.4(2) MeV [40]. Based on F extracted above, we predict $F_\pi/F = \sqrt{1/2} f_\pi/F = 1.0675(19)$.

As shown in Table X and inspired by the previous sections, the discretization error in quark mass is consistent

with zero, while this error in f_π is much more significant. On the other hand, the finite volume effect appears to be compariable with the discretization effect, with the correction on the F32P21 ensemble with the smallest $m_\pi L$ being about 4.6(1.1)%.

It is worth mentioning that the dependence of the pion mass on the strange quark mass is almost consistent with zero, as expected based on the direct calculation of the strange content in the pseudoscalar meson and the Feynman-Hellman theorem [54]. However, the dependence of the pion decay constant on the strange quark mass is more significant, which is partially attributed to the smaller uncertainty. Currently, the strange quark mass on the C24P34, C48P14, and H48P32 ensembles is higher than the physical value, while on all the other ensembles it is lower. Therefore, this dependence may arise from other systematic effects, and we cannot exclude this possibility with the present ensembles. Further studies with tuned quark masses would be helpful in verifying this.

To illustrate the lattice spacing dependence and the unitary quark mass dependence, we subtracted the partially quenching effect using bootstrap samples of the fit parameters from the original data points $m^{\rm data}_{\pi,\rm vv}$ and $f^{\rm data}_{\pi,\rm vv}$. We define the corrected $m^{\rm uni}_\pi$ and $f^{\rm uni}_\pi$ as follows:

$$\begin{aligned}(m^{\rm uni}_\pi)^2 &= \frac{(m^{\rm data}_{\pi,\rm vv})^2}{1+c_{m,L}e^{-m_\pi L}+c_{m,s}(m^2_{\eta_s}-m^2_{\eta_s,\rm phys})} \\ &\quad -\Lambda^2_\chi y_{\rm v}(y_{\rm s}-y_{\rm v})\left\{-\frac{2}{N_f}[\ln(2y_{\rm v})+1]\right. \\ &\quad \left.+2N_f(2\alpha_6-\alpha_4)\right\}(1+c_{m,a}a^2), \\ f^{\rm uni}_\pi &= \frac{f^{\rm data}_{\pi,\rm vv}}{1+c_{f,l}e^{-m_\pi L}+c_{f,s}(m^2_{\eta_s}-m^2_{\eta_s,\rm phys})} \\ &\quad -F(y_{\rm s}-y_{\rm v})\left\{-\frac{N_f}{2}\ln(y_{\rm v}+y_{\rm s})+N_f\alpha_4\right\} \\ &\quad \times(1+c_{f,a}a^2). \end{aligned} \tag{A33}$$

The m_π and f_π with unitary valence and sea quark masses $y=y_{\rm v}=y_{\rm s}$ have another widely used parametrization,

$$m^2_\pi = \Lambda^2_\chi 2y\left[1+y\left(\ln\frac{2y\Lambda^2_\chi}{m^2_{\pi,\rm phys}}-\ell_3\right)+\mathcal{O}(y^2)\right], \tag{A34}$$

$$F_\pi = F\left[1-2y\left(\ln\frac{2y\Lambda^2_\chi}{m^2_{\pi,\rm phys}}-\ell_4\right)+\mathcal{O}(y^2)\right], \tag{A35}$$

where $\ell_{3,4}$ is related to $\alpha_{4,5,6,8}$ by

$$\begin{aligned}\ell_3 &= \ln\frac{\Lambda^2_\chi}{m^2_{\pi,\rm phys}}-2[(2\alpha_8-\alpha_5)+2(2\alpha_6-\alpha_4)], \\ \ell_4 &= \ln\frac{\Lambda^2_\chi}{m^2_{\pi,\rm phys}}+\frac{1}{2}(\alpha_5+2\alpha_4). \end{aligned} \tag{A36}$$

Our determination of $\ell_{3,4}$ are also collected in Table II, consistent with the current FLAG average but have smaller uncertainties.

In this work, we use the $m_{K^\pm}$ and m_{K^0} with the constraint $m^{\rm phys}_u+m^{\rm phys}_d=2m^{\rm phys}_l$, to determine the up, down, and strange quark masses $m_{u,d,s}$. The partially quenched kaon masses and decay constants on all the ensembles are fitted with the following form proposed in a recent work [35]:

$$\begin{aligned}&m^2_K(m^{\rm v}_l,m^{\rm s}_l,m^{\rm v}_s,m^{\rm s}_s,a) \\ &=(b^{\rm v}_s m^{\rm v}_s+b^{\rm s}_s m^{\rm s}_s+b^{\rm v}_l m^{\rm v}_l+b^{\rm s}_l m^{\rm s}_l) \\ &\quad\times[1+c^K_l m^{\rm v}_l+c^K_m a^2+c^K_L\exp(-m_\pi L)], \end{aligned} \tag{A37}$$

$$\begin{aligned}&f_K(m^{\rm v}_l,m^{\rm s}_l,m^{\rm v}_s,m^{\rm s}_s,a) \\ &=(d_f+d^{\rm v}_s m^{\rm v}_s+d^{\rm s}_s m^{\rm s}_s+d^{\rm v}_l m^{\rm v}_l+d^{\rm s}_l m^{\rm s}_l) \\ &\quad\times[1+d^K_a a^2+d^K_L\exp(-m_\pi L)]. \end{aligned} \tag{A38}$$

Based on the QED correction $\Delta_{\rm QED}m_K$ obtained in previous literature [34],

$$\begin{aligned}\Delta_{\rm QED}m_{K^\pm}-\Delta_{\rm QED}m_{K^0} &= 2.07(15)\ \text{MeV}, \\ \Delta_{\rm QED}m^2_{K^0} &= 0.174(24)\times10^{-3}\ \text{GeV}^2, \end{aligned} \tag{A39}$$

we can obtain $\Delta_{\rm QED}m_{K^0}=0.17(2)$ MeV and $\Delta_{\rm QED}m_{K^\pm}=2.24(15)$ MeV, respectively. Thus, the pure QCD kaon mass with physical quark mass will be

TABLE XI. Global fit of the kaon mass and decay constant, with both $\delta_{\rm np}Z_P$ and $\delta_{\rm p}Z_P$.

χ^2/d.o.f.	b^v_l (GeV)	b^s_l (GeV)	b^v_s (GeV)	b^s_s (GeV)	c^K_l (GeV^{-1})	c^K_a(fm^{-2})	c^k_L
0.94	2.36(94)	0.23(25)	2.30(12)	0.07(13)	1.2(3.3)	1.4(4.2)	0.24(35)
χ^2/d.o.f.	d_f (GeV)	d^v_l	d^s_l	d^v_s	d^s_s	d^K_a (fm^{-2})	d^k_L
0.98	0.1291(32)	0.161(51)	0.573(49)	0.1601(80)	0.085(30)	−5.43(87)	−0.386(94)

$$m_{K^0,\mathrm{QCD}} = m_{K^0}^{\mathrm{phys}} - \Delta_{\mathrm{QED}} m_{K^0} = 497.44(02)\ \mathrm{MeV},$$
$$m_{K^\pm,\mathrm{QCD}} = m_{K^\pm}^{\mathrm{phys}} - \Delta_{\mathrm{QED}} m_{K^\pm} = 491.44(15)\ \mathrm{MeV}, \quad \text{(A40)}$$

and the physical quark masses m_u^{phys}, m_d^{phys} and m_s^{phys} can be determined using the following three conditions:

$$m_K(m_d^{\mathrm{phys}}, m_l^{\mathrm{phys}}, m_s^{\mathrm{phys}}, m_s^{\mathrm{phys}}, 0) = m_{K^0,\mathrm{QCD}},$$
$$m_K(m_u^{\mathrm{phys}}, m_l^{\mathrm{phys}}, m_s^{\mathrm{phys}}, m_s^{\mathrm{phys}}, 0) = m_{K^\pm,\mathrm{QCD}},$$
$$m_u^{\mathrm{phys}} + m_d^{\mathrm{phys}} = 2m_l^{\mathrm{phys}}. \quad \text{(A41)}$$

Note that we ignored the isospin symmetry breaking effect in the sea quark masses, since it should be $\mathcal{O}((m_d - m_u)^2)$ and negligible given the current uncertainties.

The corrected kaon mass m_K^{cr} and the decay constant f_K^{cr} shown in Fig. 4 are defined as

$$(m_K^{\mathrm{cr}})^2 = (m_K^{\mathrm{data}})^2 - m_K^2(m_l^{\mathrm{v}}, m_l^{\mathrm{s}}, m_s^{\mathrm{v}}, m_s^{\mathrm{s}}, a, L) + m_K^2(m_l^{\mathrm{phys}}, m_l^{\mathrm{phys}}, m_s^{\mathrm{v}}, m_s^{\mathrm{v}}, a, L \to \infty), \quad \text{(A42)}$$

$$f_K^{\mathrm{cr}} = f_K^{\mathrm{data}} - f_K(m_l^{\mathrm{v}}, m_l^{\mathrm{s}}, m_s^{\mathrm{v}}, m_s^{\mathrm{s}}, a, L) + f_K(m_l^{\mathrm{phys}}, m_l^{\mathrm{phys}}, m_s^{\mathrm{v}}, m_s^{\mathrm{v}}, a, L \to \infty), \quad \text{(A43)}$$

with the light quark mass m_l corrected to its physical value m_l^{phys} using the bootstrap samples of the fitted m_K.

As a consistency check, we also calculate m_{η_s} on each ensemble and perform a similar global fit with the following functional form:

$$m_{\eta_s}^2 = [h_l^{\mathrm{s}} m_l^{\mathrm{s}} + h_s^{\mathrm{v}} m_s^{\mathrm{v}} + h_s^{\mathrm{s}} m_s^{\mathrm{s}} + h_{l^2}(m_l^{\mathrm{s}})^2] \times (1 + h_a a^2 + h_L e^{m_{\eta_s} L}), \quad \text{(A44)}$$

The χ^2/d.o.f. of the fit is 1.4 an all the coefficients except h_s^l are consistent with zero within the uncertainty, but dropping more terms will enlarge the χ^2/d.o.f. significantly and then we keep all the coefficients. Using the physical light and strange quark masses, we predict $m_{\eta_s} = 687.4(2.2)$ MeV in the infinite volume and continuum limit, which is consistent with the BMWc value of 689.63 (18) MeV [48] we used in the fits for lattice spacing and f_π. Additively, we extract the dependence of $m_{\eta_s}^2$ on the strange quark mass, $\frac{\partial m_{\eta_s}^2}{\partial m_s} = 4.9(1)$ GeV, which is slightly lower than the value of m_π^2/m_q shown in Fig. 3.

The physical quark masses $m_{u,d,s}$ and also corresponding $f_{\pi,K}$ using m_l^{phys} and intermediate RI/MOM scheme, are collected in Table II. In addition, Table II shows the global-fit results using the $z_{A,P}$ through the SMOM scheme for comparison. As we can see from the continuum extrapolation tests using a 317 MeV pion mass, the SMOM scheme yields quark masses that are 3–4% lower and decay constants that are ∼2% lower compared to the RI/MOM scheme. However, the ratio of the quark masses or decay constants remains unchanged within the uncertainty as the renormalization constants are canceled.

Therefore, we consider the result using the RI/MOM scheme as the central value due to its smaller discretization error, and treat the difference between the results obtained using the two schemes as systematic uncertainties. Such a systematic uncertainty can also be considered as an estimate of the residual discretization error, as the correct continuum limit should be independent of the intermediate renormalization scheme. With this systematic uncertainty, all our determinations are consistent with the present lattice averages [26] and/or PDG [40] within $1-2\sigma$, and the low-energy constants Σ and $\ell_{3,4}$ have smaller uncertainties.

[1] C. Aubin, C. Bernard, C. E. DeTar, J. Osborn, S. Gottlieb, E. B. Gregory, D. Toussaint, U. M. Heller, J. E. Hetrick, and R. Sugar (MILC Collaboration), Phys. Rev. D **70**, 114501 (2004).
[2] C. Aubin *et al.* (HPQCD, MILC, and UKQCD Collaborations), Phys. Rev. D **70**, 031504 (2004).
[3] Q. Mason, H. D. Trottier, R. Horgan, C. T. H. Davies, and G. P. Lepage (HPQCD Collaboration), Phys. Rev. D **73**, 114501 (2006).
[4] A. Bazavov *et al.* (MILC Collaboration), Proc. Sci. CD09 (**2009**) 007 [arXiv:0910.2966].
[5] C. T. H. Davies, C. McNeile, K. Y. Wong, E. Follana, R. Horgan, K. Hornbostel, G. P. Lepage, J. Shigemitsu, and H. Trottier, Phys. Rev. Lett. **104**, 132003 (2010).
[6] A. Bazavov *et al.* (MILC Collaboration), Rev. Mod. Phys. **82**, 1349 (2010).
[7] J. Laiho and R. S. Van de Water, Proc. Sci. LATTICE2011 (2011) 293 [arXiv:1112.4861].
[8] C. McNeile, C. T. H. Davies, E. Follana, K. Hornbostel, and G. P. Lepage, Phys. Rev. D **82**, 034512 (2010).
[9] S. Basak *et al.* (MILC Collaboration), Proc. Sci. LATTICE2015 (**2016**) 259 [arXiv:1606.01228].
[10] Y. Maezawa and P. Petreczky, Phys. Rev. D **94**, 034507 (2016).
[11] A. Bazavov *et al.*, Phys. Rev. D **98**, 074512 (2018).
[12] A. Bazavov *et al.* (Fermilab Lattice, MILC, and TUMQCD Collaborations), Phys. Rev. D **98**, 054517 (2018).
[13] S. Basak *et al.* (MILC Collaboration), Phys. Rev. D **99**, 034503 (2019).
[14] C. Allton *et al.* (RBC-UKQCD Collaboration), Phys. Rev. D **78**, 114509 (2008).

[15] Y. Aoki *et al.* (RBC and UKQCD Collaborations), Phys. Rev. D **83**, 074508 (2011).
[16] T. Blum, R. Zhou, T. Doi, M. Hayakawa, T. Izubuchi, S. Uno, and N. Yamada, Phys. Rev. D **82**, 094508 (2010).
[17] R. Arthur *et al.* (RBC and UKQCD Collaborations), Phys. Rev. D **87**, 094514 (2013).
[18] T. Blum *et al.* (RBC and UKQCD Collaborations), Phys. Rev. D **93**, 074505 (2016).
[19] Y.-B. Yang *et al.*, Phys. Rev. D **92**, 034517 (2015).
[20] T. Ishikawa *et al.* (JLQCD Collaboration), Phys. Rev. D **78**, 011502 (2008).
[21] S. Sint, Nucl. Phys. **B847**, 491 (2011).
[22] S. Aoki *et al.* (PACS-CS Collaboration), Phys. Rev. D **79**, 034503 (2009).
[23] S. Aoki *et al.* (PACS-CS Collaboration), Phys. Rev. D **81**, 074503 (2010).
[24] S. Aoki *et al.* (PACS-CS Collaboration), J. High Energy Phys. 08 (2010) 101.
[25] S. Aoki *et al.*, Phys. Rev. D **86**, 034507 (2012).
[26] Y. Aoki *et al.* (Flavour Lattice Averaging Group (FLAG) Collaboration), Eur. Phys. J. C **82**, 869 (2022).
[27] M. Bruno, I. Campos, P. Fritzsch, J. Koponen, C. Pena, D. Preti, A. Ramos, and A. Vladikas (ALPHA Collaboration), Eur. Phys. J. C **80**, 169 (2020).
[28] S. Durr, Z. Fodor, C. Hoelbling, S. D. Katz, S. Krieg, T. Kurth, L. Lellouch, T. Lippert, K. K. Szabo, and G. Vulvert (BMW Collaboration), J. High Energy Phys. 08 (2011) 148.
[29] G. Martinelli, C. Pittori, C. T. Sachrajda, M. Testa, and A. Vladikas, Nucl. Phys. **B445**, 81 (1995).
[30] Y. Aoki *et al.*, Phys. Rev. D **78**, 054510 (2008).
[31] C. Sturm, Y. Aoki, N. H. Christ, T. Izubuchi, C. T. C. Sachrajda, and A. Soni, Phys. Rev. D **80**, 014501 (2009).
[32] N. Hasan, J. Green, S. Meinel, M. Engelhardt, S. Krieg, J. Negele, A. Pochinsky, and S. Syritsyn, Phys. Rev. D **99**, 114505 (2019).
[33] N. Carrasco *et al.* (European Twisted Mass Collaboration), Nucl. Phys. **B887**, 19 (2014).
[34] D. Giusti, V. Lubicz, C. Tarantino, G. Martinelli, F. Sanfilippo, S. Simula, and N. Tantalo, Phys. Rev. D **95**, 114504 (2017).
[35] C. Alexandrou *et al.* (Extended Twisted Mass Collaboration), Phys. Rev. D **104**, 074515 (2021).
[36] M. Lüscher, J. High Energy Phys. 08 (2010) 071; 03 (2014) 92(E).
[37] S. Borsanyi *et al.* (BMW Collaboration), J. High Energy Phys. 09 (2012) 010.
[38] F. He, Y.-J. Bi, T. Draper, K.-F. Liu, Z. Liu, and Y.-B. Yang (χQCD Collaboration), Phys. Rev. D **106**, 114506 (2022).
[39] X. Feng, L. Jin, and M. J. Riberdy, Phys. Rev. Lett. **128**, 052003 (2022).
[40] P. A. Zyla *et al.* (Particle Data Group), Prog. Theor. Exp. Phys. **2020**, 083C01 (2020).
[41] S. R. Sharpe, Phys. Rev. D **56**, 7052 (1997); **62**, 099901(E) (2000).
[42] M. Della Morte, R. Hoffmann, and R. Sommer, J. High Energy Phys. 03 (2005) 029.
[43] R. G. Edwards and B. Joo (SciDAC, LHPC, and UKQCD Collaborations), Nucl. Phys. B, Proc. Suppl. **140**, 832 (2005).
[44] M. A. Clark, R. Babich, K. Barros, R. C. Brower, and C. Rebbi, Comput. Phys. Commun. **181**, 1517 (2010).
[45] R. Babich, M. A. Clark, B. Joo, G. Shi, R. C. Brower, and S. Gottlieb, in *Proceedings of the SC11 International Conference for High Performance Computing, Networking, Storage and Analysis Seattle, Washington, 2011* (Association for Computing Machinery, New York, NY, 2011), https://doi.org/10.1145/2063384.2063478.
[46] M. A. Clark, B. Jo, A. Strelchenko, M. Cheng, A. Gambhir, and R. Brower, arXiv:1612.07873.
[47] Y.-J. Bi, Y. Xiao, W.-Y. Guo, M. Gong, P. Sun, S. Xu, and Y.-B. Yang, Proc. Sci. LATTICE2019 (**2020**) 286 [arXiv:2001.05706].
[48] S. Borsanyi *et al.*, Nature (London) **593**, 51 (2021).
[49] J. A. Gracey, Eur. Phys. J. C **83**, 181 (2023).
[50] K. Zhang, Y.-Y. Li, Y.-K. Huo, A. Schäfer, P. Sun, and Y.-B. Yang (χQCD Collaboration), Phys. Rev. D **104**, 074501 (2021).
[51] L. Chang, Y.-B. Liu, K. Raya, J. Rodríguez-Quintero, and Y.-B. Yang, Phys. Rev. D **104**, 094509 (2021).
[52] J. Gasser and H. Leutwyler, Nucl. Phys. **B250**, 465 (1985).
[53] P. Boyle *et al.*, Phys. Rev. D **93**, 054502 (2016).
[54] Y.-B. Yang, Y. Chen, T. Draper, M. Gong, K.-F. Liu, Z. Liu, and J.-P. Ma, Phys. Rev. D **91**, 074516 (2015).